WILEY-VCH

DOI: 10.1002/ ((please add manuscript number))
Article type: Progress Report

Recent advances in perovskite oxides as electrode materials for non-aqueous lithium-oxygen batteries

Peng Tan, Meilin Liu, Zongping Shao, Meng Ni**

Dr. Peng Tan[a], Prof. Meng Ni[a,b]
[a] Department of Building and Real Estate, The Hong Kong Polytechnic University, Hung Hom, Kowloon, Hong Kong, China
[b] Environmental Energy Research Group, Research Institute for Sustainable Urban Development (RISUD), The Hong Kong Polytechnic University, Hung Hom, Kowloon, Hong Kong, China
E-mail: pengtan1990@hotmail.com (Peng Tan) bsmengni@polyu.edu.hk (Meng Ni)
Prof. Meilin Liu[c]
[c] School of Materials Science and Engineering, Center for Innovative Fuel Cell and Battery Technologies, Georgia Institute of Technology, Atlanta, GA 30332-0245, USA
E-mail: meilin.liu@mse.gatech.edu (Meilin Liu)
Prof. Zongping Shao[d,e]
[d] Jiangsu National Synergetic Innovation Center for Advanced Material, College of Energy, State Key Laboratory of Materials-Oriented Chemical Engineering, Nanjing Tech University, Nanjing 210009, China
[e] Department of Chemical Engineering, Curtin University, Perth, WA 6845, Australia
Email: zongping.shao@curtin.edu.au (Zongping Shao)

Keywords: perovskite oxide, oxygen electrode, non-aqueous lithium-oxygen battery, mechanism, structure

Lithium-oxygen batteries are considered the next generation power sources for many applications. The commercialization of this technology, however, is hindered by a variety of technical hurdles, including low obtainable capacity, poor energy efficiency, and limited cycle life of the electrodes, especially the cathode (or oxygen) electrode. During the last decade, tremendous efforts have been devoted to the development of new cathode materials. Among them, perovskite oxides have attracted much attention due to the extraordinary tunability of their compositions, structures, and functionalities (e.g., high electrical conductivities and catalytic activities), demonstrating the potential to achieve superior battery performance. This article focuses on the recent advances of perovskite oxides as the electrode materials in non-aqueous lithium-oxygen batteries. The electrochemical mechanisms of oxygen reduction reaction (ORR) and oxygen evolution reaction (OER) on the surface of perovskite oxides are

first summarized. Then, the effect of nanostructure and morphology on ORR and OER activities is reviewed, from nanoparticles to hierarchical porous structures. Moreover, perovskite oxide-based composite electrodes are discussed, highlighting the enhancement in electrical conductivities, catalytic activities, and durability under realistic operating conditions. Finally, the remaining challenges and new directions for achieving rational design of perovskite oxides for non-aqueous lithium-oxygen batteries are outlined and discussed.

1. Introduction

Low-cost and efficient electric energy storage systems are urgently needed to meet the ever-increasing demand for clean energy. For now and the forseable future, batteries, fuel cells, and supercapacitors are among the best options.[1,2] For example, lithium-ion batteries (LIBs) have demonstrated reasonable energy density (theoretical value: ~400 Wh kg^{-1}), cycle life (>5000 cycles), and energy efficiency (>90%).[3] As a result, LIBs have been used as the power source for electric vehicles, achieving a driving distance of ~400 km per charge.[4] Despite the progress accomplished to date, however, the specific energy densities of LIBs are still far inferior to that of the conventional gasoline engines (~13,000 Wh kg^{-1}).[5] Thus, the exploitation of new energy storage technologies with higher energy density is still a grand challenge.

In attempts to dramatically enhance energy density, much attention has been devoted to metal-air batteries, especially lithium-air, aluminum-air, and zinc-air batteries.[6] In this type of batteries, a metal is used as the electrode rather than an intercalation compound such as $LiFePO_4$, while the active component, oxygen, can be obtained from ambient air, minimizing the required mass and volume of the air electrode and increasing the energy density of the battery. Among the metal-air batteries, the lithium-air battery (LAB) has garnered the most attention, largely due to the lowest equivalent weight of lithium metal. The theoretical capacity of lithium is 3,862 Ah kg^{-1}, corresponding to an energy density of ~11,680 Wh kg^{-1}

for a cell voltage of about 3.0 V.[7] This theoretical energy density is approaching that of gasoline, showing the remarkable potential of LABs for future power sources.

The operation of a LAB involves lithium dissolution and deposition on the negative (or lithium) electrode and oxygen reduction reaction (ORR) and oxygen evolution reaction (OER) on the positive (or air) electrode.[8] Since the demonstration of a prototype rechargeable LAB by Abraham and Jiang in 1996,[9] many advancements have been made due to worldwide attention devoted to LABs. In terms of electrolytes used, four types of LABs have been proposed and developed, including non-aqueous, aqueous, hybrid non-aqueous/aqueous, and solid-state LABs.[10] Among them, the non-aqueous system is the most widely developed one owing to its high-reversible capacity.[11] A typical non-aqueous LAB consists of a lithium metal electrode, a porous air electrode with active materials, and an electrolyte made of lithium salt in an aprotic solvent, as schematically shown in **Figure 1a**. In order to prevent the internal short-circuit between the anode and the cathode, a separator is usually used between them. During discharge, lithium metal is oxidized at the anode, producing electrons and lithium ions, as oxygen is reduced at the cathode by electrons transported through an external circuit and combined with lithium ions transported via the electrolyte to form lithium peroxide (Li_2O_2). The electrochemical reaction occurring on the positive electrode is summarized in Equation 1. Since Li_2O_2 has limited solubility in a non-aqueous electrolyte, it deposits on the surface of a porous cathode. During charge, the electrochemical process is reversed; the solid Li_2O_2 is electrochemically oxidized at the positive (or air) electrode, producing electrons, lithium ions, and O_2.

$$2Li^+ + 2e^- + O_2 \underset{\text{Charge}}{\overset{\text{Discharge}}{\rightleftharpoons}} Li_2O_2 \ (E^0 = 2.96 \text{ V vs. } Li/Li^+) \quad (1)$$

However, a wide variety of technical hurdles must be overcome to make LAB technology commercially viable. As schematically shown in Figure 1b, the obtainable discharge capacity is usually lower than the expected value due to poor utilization of the pore

volume,[12] and dramatically decreases with an increase in the current density.[13] Besides, the charge overpotential is usually high (~1.0 V), resulting in poor energy efficiency (<70%).[13] Moreover, the capacity greatly decreases with an increase in the cycle number, leading to limited cycle life (<500 cycles). Apart from the above-mentioned issues, most reported LABs were operated in a pure oxygen atmosphere rather than ambient air to avoid contaminations from air (e.g., CO_2, H_2O),[14] which may react with cell components to form irreversible side products,[15] leading to rapid degradation in performance or even failure in operation.[16] Hence, the term "lithium-oxygen" is commonly used instead of "lithium-air" in the literature.[17] Unless specified otherwise, the battery performances reported in this article are acquired under oxygen atmosphere; accordingly, we use the term "lithium-oxygen battery (LOB)" in the following discussion.

To overcome these technical difficulties, it is necessary to gain a profound understanding of the electrochemical processes in LOBs and to develop new battery materials that can facilitate the desirable electrochemical reactions while tolerating to contaminations commonly encountered in battery operation. For instance, carbonate-based electrolytes (e.g., ethylene carbonate, EC; dimethyl carbonate, DEC; dimethyl carbonate, DMC) were used in the early stage development of non-aqueous LOBs because they are widely used in LIBs.[18-21] It was quickly found that the discharge products are irreversible lithium carbonate and alkylcarbonate rather than Li_2O_2 due to the decomposition of electrolytes,[22,23] leading to poor cycle life. Accordingly, other non-aqueous electrolyte systems with improved stabilities against superoxide radicals and oxidation potentials were formulated to ensure longer cycle life, including dimethoxyethane (DME),[24-28] tetraethylene glycol dimethyl ether (TEGDME),[29-39] and dimethyl sulfoxide (DMSO).[40-42] As both ORR and OER occur in the porous positive (or oxygen) electrode, the architecture of this electrode is vital to its performance. To enhance the rate capability while maintaining high capacity, the microstructure of the electrode should be designed to maximize the length of the triple-phase

boundaries among oxygen, lithium ions, and electrons. To facilitate the discharge/charge reactions and improve the energy efficiency, the oxygen electrode should have a high electrical conductivity and electrocatalytic activities. In addition, to achieve a long cycle life, the electrode should be stable in the oxidizing environment. Since the high charge overpotential in LOBs not only results in poor energy efficiency, but also causes the decomposition of electrolyte and electrode materials, the exploration of effective methods to decrease the charge voltage is especially crucial. To date, various kinds of materials have been studied as the electrode materials, including carbons,[43-45] metals,[46-52] metal oxides,[53-67] and others,[68-72] and some striking improvements have been achieved. For example, an air electrode made of RuO_2 hollow spheres enabled an average charge voltage as low as 3.59 V;[73] a Pt_3Co nanocube catalyst exhibited a low charge potential of 3.1 V with a high energy efficiency of ~86.5%.[74] However, the high cost of noble metals or metal oxides (e.g., Pt, Ru, RuO_2) is a significant limitation to the large-scale commercialization.[75-81] In addition, the redox mediator (RM), which acts as an electron-hole transfer agent that permits efficient oxidation of solid Li_2O_2, has been developed.[82-87] A soluble lithium iodide (LiI) catalyst could achieve a low overpotential of only 0.25 V, with stable and reversible cycling for more than 900 times.[84] However, the RM can cause side reactions in the air electrode and the lithium electrode,[87] resulting in complex influences on the battery performance. Hence, searching for low-cost electrode materials with high-performance still requires tremendous efforts, among which perovskite oxides have attracted great attention.

Perovskite oxides have a general chemical formula of ABO_3, where A is a rare-earth (e.g., La) or alkaline-earth cation and B is a transition-metal cation (e.g., Mn, Co, Fe).[88] An perfect perovskite has a cubic structure, as schematically shown in **Figure 2**. In reality, however, the crystal structure may be distorted to tetragonal, orthorhombic, or rombohedral structure due to the variation or substitution of A and/or B cations with different sizes and valencies.[89] By partial substitution of cations at A and/or B sites, a variety of perovskite

compounds can be obtained with the formula $A_{1-x}A'_xB_{1-y}B'_yO_{3\pm\delta}$, where "+" denotes oxygen excess and "–" denotes oxygen deficiency.[89] The properties of perovskite oxides can vary in a wide range by partially replacing A and/or B cations with other metal ions. To date, A site substitution has been successfully used to tailor the oxygen stoichiometry and conductivity of perovskite materials whereas B site substitution to tune the catalytic activity of the materials.[90,91] For instance, substituting La with an alkaline-earth element (e.g., Sr, Ca) at the A site introduces oxygen nonstoichiometry into the perovskite structure, resulting in a high electrical conductivity.[92] While the cations on the B site have been found to play essential roles in altering the electronic structure of the perovskite oxides, and substituting B cations with a reducible early transition metal (e.g., Co, Mn) provides redox active sites to facilitate catalytic reactions.[93,94]

Due to the unique tailorable and tunable physi-chemical properties, such as crystal structures, electrical conductivity, and ionic conductivity, perovskite oxides have been regarded as the most promising materials for many energy conversion and storage systems.[95] For instance, the cathode materials for solid oxide fuel cells (SOFCs) require high electrical conductivity and high electrocatalytic activity for the ORR, as well as a high diffusivity for the transfer of oxygen anions.[96,97] To this end, perovskite oxides, especially with mixed electronic and ionic conductivities, such as $Ba_{0.5}Sr_{0.5}Co_{0.8}Fe_{0.2}O_{3-\delta}$ and $La_{0.6}Sr_{0.4}Co_{0.2}Fe_{0.8}O_{3-\delta}$, have been intensively investigated.[98] It is found that the compound with Ba and Sr on the A site exhibits the fastest O-ion transport kinetics, while the B site with the Co-rich compositions displays faster kinetic coefficients than the Fe-rich compositions.[99] In addition, perovskite oxides with several key properties, including flexibility in the oxidation states of transition metals (e.g., B^{m+}/B^{m+1}), defective structures for oxygen vacancy or excess, excellent oxygen anion mobility, and excellent oxygen exchange kinetics,[100] make them excellent candidates as bifunctional catalysts in alkaline fuel cells[101] and metal-air

batteries.[102] Focused on these applications, dozens of reviews have been published.[100] Perovskite oxides are ideally suited for LOBs since they have the most desirable properties for an electrode material: high electrical conductivities, good catalytic activities, and low-cost. Although different kinds of electrode materials for LOBs have been reviewed so far,[103-109] the applications of perovskite oxides have not yet been systematically summarized. In this article, we focus on the recent advances in the development of perovskite oxides as the electrode materials for LOBs. The remaining part of this review is organized as follows: Section 2 introduces the fundamental understanding of the oxygen electrochemistry in non-aqueous electrolytes and the proposed mechanisms of ORR and OER on the surface of perovskite oxides; Section 3 summarizes the application of various perovskite oxides as the electrode materials, from nanoparticles to hierarchical porous structures; Section 4 reviews the perovskite oxide-based composites, highlighting the enhancement in electrical conductivities, catalytic activities, and durability under realistic operating conditions; and Section 5 outline and discuss the remaining challenges and new directions for achieving rational design of perovskite oxides for LOBs.

2. Mechanism investigation

Understanding the electrochemical reactions gives an important implication to design and fabricate effective electrode materials for LOBs. In this section, we review the previous reports that elaborate the oxygen electrochemistry and propose the mechanisms on perovskite oxides. First, the mechanisms of oxygen reduction in non-aqueous LOBs and the corresponding influences on the discharge capacity are introduced. Then, different oxygen evolution mechanisms considering the product morphology and structure are summarized. Moreover, the effects of perovskite oxides on the oxygen reduction and evolution processes and the design principles are discussed.

2.1. Oxygen reduction reaction

In alkaline fuel cells and metal-air batteries (e.g., zinc-air battery), the ORR process in basic solutions can be expressed as:

$$O_2 + 2H_2O + 4e^- \rightarrow 4OH^- \quad (2)$$

where the formed product (OH^-) is dissovled in the aqueous solutions. While in LOBs, as expressed in Equation 1, the discharge product (Li_2O_2) is in the solid state. The typical hypothesized route was proposed by Abraham and co-workers,[40,110] which involves the reduction of oxygen as:

$$O_2 + e^- \rightarrow O_2^- \quad (3)$$

and combines with lithium ion (Li^+) to form lithium superoxide (LiO_2):

$$O_2^- + Li^+ \rightarrow LiO_2 \quad (4)$$

followed by

$$2LiO_2 \rightarrow Li_2O_2 + O_2 \quad (5)$$

and/or

$$LiO_2 + Li^+ + e^- \rightarrow Li_2O_2 \quad (6)$$

Oxygen dissolved in the electrolyte first reduces through a one-electron transfer (Equation 3) to form LiO_2. Subsequently, LiO_2 can undergo a disproportionation reaction (Equation 5) or another one-electron-transfer electrochemical process (Equation 6) to form solid Li_2O_2.

Various Li_2O_2 morphologies have been observed in LOBs with different materials and operating conditions, including film,[12,111,112] toroid,[113,114] disc,[115] particle,[116] and other shapes.[117,118] The different morphologies suggest the different oxygen reduction mechanisms.[119] Bruce *et al.* showed that the solvent property, donor number (DN), influences O_2 reduction through its effect on the solubility of LiO_2.[120] Two different mechanisms, the solution mechanism and the surface mechanism, have been proposed, as schemed in **Figure 3**.[121] After the formation of LiO_2, an equilibrium exists between LiO_2 adsorbed on the electrode and LiO_2 dissolved in the electrolyte solution, and the detail mechanism is governed by the competition between the LiO_2 solubility and the adsorption

free energy of LiO_2 on the oxygen electrode surface. In the surface mechanism, two sequential one-electron transfer steps yield insoluble Li_2O_2 at the electrode surface, resulting in a Li_2O_2 film growth on the electrode. Due to the low electrical conductivity of Li_2O_2,[122] the voltage decays with the coverage of the Li_2O_2 film, leading to a capacity corresponding to a Li_2O_2 layer of ~5–6 nm at the end of discharge and thus a low utilization of pore volumes of the electrode. In the solution mechanism (e.g., in high-DN solvents), two soluble LiO_2 molecules disproportionate[123] or through a one-electron electrochemical process to form Li_2O_2. In this case, discharge continues far beyond the electrical conductivity limitation because most Li_2O_2 grows from solution, resulting in the formation of large Li_2O_2 particles and the improved utilization of the pore volumes. Consequently, at a same discharge condition (e.g., a low overpotential) the solution mechanism with the formation of large-sized Li_2O_2 can lead to specific capacities several times higher than those of the surface mechanism with film-like Li_2O_2.[124] For electrolyte, both the solvent and the dissolved lithium salt can determinate the LiO_2 solubility,[125-127] affecting the reaction route. While for a given electrolyte, different electrode surfaces have different adsorption energies, and therefore play a key role in determining the oxygen reduction mechanism and the discharge performance.[128-131]

To investigate the influence of pervoskite oxides on the ORR process, Mai *et al.* tested the performance of $La_{0.5}Sr_{0.5}CoO_{2.91}$ (LSCO) as the catalyst in a carbonate-based electrolyte, and found that the discharge capacity increased compared with that of the pristine carbon electrode.[132] They proposed the ORR mechanism on LSCO as follows: since the oxygen reduction (Equation 3) is the rate-controlling step, the oxygen chemisorption and O_2^- desorption should be the influence factors. O_2 and Co ions may be functionally similar to Lewis acid and Lewis base sites, respectively. Here, Co ions can serve as an active center for O_2 chemisorption. CoO_6 species with e_g electrons can donate electrons to σ^*2p orbitals of O_2, and the t_{2g} electrons of Co ions can interact with π^*2p electrons of O_2 to form a π-bond. Thus,

the bond strength and oxygen chemisorption can be increased. Additionally, oxygen vacancies in the LSCO catalyst can decrease the repulsion between adsorbed O and lattice O, leading to enhanced oxygen chemisorption. However, the carbonate-based electrolytes were proved to be unstable in the ORR process of LOBs,[18-21] concealing the real role of LSCO in the electrode. Chi *et al.* used $La_{0.6}Sr_{0.4}Co_{0.2}Fe_{0.8}O_3$ (LSCF) as the catalyst in a DMSO-based electrolyte, and found that different from pristine Ketjen black (KB) electrode in which the product Li_2O_2 is compact plate-like, the LSCF-KB electrode led to a changed Li_2O_2 morphology of tiny leaf-like with three-dimensional (3D) structure coated on the surface with an increased discharge capacity.[133] The morphology difference was explained through the different oxygen reduction mechanisms as shown in **Figure 4**. Many oxygen vacancies are formed in the LSCF nanostructure, which can accelerate the dissociation of oxygen molecules on the surface and increase the mobility of lattice oxygen. In addition, LSCF can provide more active sites. As a result, both the transfer pathway of oxygen and the Li_2O_2 nucleation sites will increase with the assistance of LSCF, accelerating the accumulation of intermediate product LiO_2. Then, LiO_2 will interact with each other to form the final products Li_2O_2 (Equation 5), which produce O_2 and the existence of LSCF can also promote the quick desorption of O_2, resulting in the formation of more Li_2O_2. Due to the limitation of LSCF active sites on LSCF-KB surface, Li_2O_2 will grow in the limited directions and results in the formation of leaf-like particles on LSCF sites rather than on KB. While in KB electrode, since the surface active sites are insufficient, the nucleation would occur randomly and lead to the slow and heterogeneous growth of Li_2O_2 overspreads the KB surface.

Although the changes of product morphology illustrated the different ORR mechanisms when introducing perovskite oxides, how to choose the suitable perovskite oxides with high activities is still challenging. In alkaline electrolytes and SOFCs, the oxygen reduction activities for various perovskite oxides have been intensively studied. For instance, Shao-Horn *et al.* found that in alkaline solutions the ORR activity for perovskite oxides primarily

correlates to σ*-orbital (e_g) occupation and the extent of B-site transition-metal-oxygen covalency.[134] The e_g-filling was taken as the ORR activity descriptor of perovskite-based oxides. Too little e_g-filling can result in B−O_2 bonding that is too strong, whereas to much e_g-filling can lead to an O_2 interaction that is too weak; neither situation is optimum for ORR activity. Thus, the electronic structure is important in controlling oxide catalytic activity, and a moderate amount of e_g-filling (~1) yields the highest activity (e.g., $La_{0.5}Ca_{0.5}MnO_3$, $LaCoO_3$ and $LaNiO_3$). Based on this molecular orbital principle, a novel perovskite oxide $La(Co_{0.55}Mn_{0.45})_{0.99}O_{3-\delta}$ (LCMO), with e_g-filling of 1, was designed by Liu *et al.*[135] As nitrogen-doped graphene has the features of good catalytic activity, high electrical conductivity, large surface area, and good chemical stability and is widely applied to grow or attach nanostructured catalysts,[136] They further integrated the LCMO with nitrogen-doped reduced graphene oxide (NrGO) by establishing an effective electrically percolating network and leveraging the unique chemical properties of NrGO. The LCMO/NrGO hybrid catalyst exhibited comparable ORR activity with 30 wt% Pt/C. More importantly, the LCMO has 1% B-site vacancy,[137] which can meanwhile confer good OER activity that can be comparable to 20wt% Ir/C. Morgan *et al.* used density functional theory (DFT) calculations to identify the O *p*-band center as a descriptor.[138] Their results suggested that a higher *p*-band center relative to the Fermi level (e.g., $Ba_{0.5}Sr_{0.5}Co_{0.75}Fe_{0.25}O_3$) is correlated with higher ORR performance for SOFC cathode applications. Even with these important findings, however, the oxygen reduction activities of various perovskite oxides in non-aqueous systems have not been systematically investigated yet. In addition, different from the case in aqueous solutions where the product is soluble, the solid product in non-aqueous electrolytes can cover the surface and affect the active sites. Thus, the microstructure of perovskite oxides plays a more significant role than that in aqueous solutions and should be considered. Moreover, the operating conditions (e.g., current density, temperature) can alter the transport and reaction

kinetics and affect the discharge performance.[139] Hence, the selection of perovskite oxides should also take the specific operating condition into account.

2.2. Oxygen evolution reaction

To make batteries rechargeable, electrochemically decomposition of solid Li_2O_2 to lithium and oxygen is required. The reaction during charge is thought to be:[10]

$$Li_2O_2 \rightarrow 2Li^+ + 2e^- + O_2 \quad (7)$$

and/or

$$Li_2O_2 \rightarrow Li^+ + e^- + LiO_2 \quad (8)$$

where Equation 7 is a two-electron process, while Equation 8 is a one-electron process involves the formation of LiO_2.[140] Although both routes are electrochemical reactions, in a practical LOB, the charge overpotential is surprisingly high,[13] which may be caused by the insulator nature of bulk Li_2O_2.[141] Hence, elucidating the OER process in non-aqueous electrolytes is the key to designing the oxygen electrode materials for decreasing the overpotential.[142,143]

Till now, many mechanisms focused on Li_2O_2 oxidation have been proposed. McCloskey *et al.* charged Li_2O_2 in a DME-based electrolyte, and found that Pt and Au supported Vulcan carbon (VC) and metal oxide (α-MnO_2 nanowires mixed into VC) catalysts did not lower the OER potential compared to pure carbon. Moreover, the onset potential at which oxygen evolution occurs was nearly identical for all electrodes, making the efficiency of electrocatalysts in LOBs questionable.[24] As the batteries under their test were only discharged to a very small capacity (~130 mAh g_{carbon}^{-1}) which might only be representative of the very initial charging behavior, Shao-Horn *et al.* used electrodes consisting of non-catalyzed and catalyzed VC and chemically synthesized Li_2O_2 with a large capacity to examine the different activities of catalysts towards OER.[144] They found that Pt and Ru nanoparticles supported on VC could significantly increase the kinetics of the Li_2O_2 oxidation. They also proposed three major reaction stages upon the charge process, as shown in **Figure**

5.[145] The first stage is the oxidation of the first sub-nanometer layer of Li_2O_2 through the delithiation process to form lithium-deficient $Li_{2-x}O_2$ and chemically disproportionate to evolve O_2 (Equation 8), followed by the oxidation of bulk Li_2O_2 to form Li^+ and O_2 (Equation 7), and ended with the oxidation of parasitic carbonates and electrolytes. They further investigated the oxygen evolution kinetics of two classes of Li_2O_2 structures, Li_2O_2 discs and particles, which are formed at high and low potentials, respectively.[28] During charge, Li_2O_2 discs consisting predominantly of O-rich (0001) surfaces with LiO_2-like electronic states exhibit limited capacity (~200 mAh g_{carbon}^{-1}) in the sloping region. In contrast, Li_2O_2 particles consisting of less O-rich surfaces (e.g, $(1\bar{1}00)$ facets[115]) exhibit a significantly enhanced (~400 mAh g_{carbon}^{-1}) sloping region with lower charge overpotentials for a given amount of Li extracted. The lower charge overpotentials of particles with proposed $(1\bar{1}00)$ and less O-rich surfaces compared to discs with (0001) surfaces are consistent with the results from DFT calculations, from which the $(1\bar{1}00)$ surfaces have lower predicted kinetic overpotentials (0.15–0.2 V) on charge compared to the oxygen-rich (0001) surfaces (0.36 V).[146] After the complete delithiation and removal of the surfaces of discs and particles with exposing the interior bulk Li_2O_2, the charge proceeds through a two-phase process (e.g., Li_2O_2 and LiO_2) for both structures with similar overpotentials. Nazar *et al.* used *operando* X-ray diffraction to observe the oxidation of Li_2O_2, and found that in contrast to the one step for bulk crystalline Li_2O_2, the oxidation of electrochemically generated Li_2O_2 occurs in the first oxidation through a non-crystalline Li_2O_2 component; followed by the crystalline peroxide *via* a Li deficient solid solution phase ($Li_{2-x}O_2$).[147] As the electrochemical formation of Li_2O_2 involves LiO_2 (Equation 5 and 6), the discharge product formed by a combination of an oxygen-rich component with superoxide-like character and a Li_2O_2 component has been illustrated, and the ratio changes with discharge current and depth and results in different product

morphologies.[148-150] In addition, the oxygen-rich superoxide-like component has a much lower charge potential (3.2−3.5 V) than that of the Li_2O_2 component (~4.2 V).[148] Xia *et al.* investigated the Li_2O_2 morphology evolution and the effects on the oxygen evolution kinetics.[151] The insulating Li_2O_2 particles with a disc-like shape are formed in the initial discharge stage, and give a high charge voltage at 4.1 V. Afterward, the nucleation and growth of Li_2O_2 crystallites at higher discharge capacities result in the electrically conducting Li_2O_2 shells that covers the cores, leading to a lower voltage range of 3.3 to 4.1 V. When the discharge voltage further drops below 2.65 V, the defective superoxide-structured phase with high conductivity is formed on the rims of Li_2O_2, making Li_2O_2 discs evolve to toroid-shaped particles and causing a comparably low charge plateau below 3.4 V.

From the investigations of OER mechanisms, several important messages can be obtained. First, the Li_2O_2 structure plays a significant role in the charge performance. The solid Li_2O_2 with different exposed surfaces shows different charge characters.[28] In addition, an oxygen-rich component with superoxide-like character and a Li_2O_2 component can co-exist in the product, and a larger ratio of LiO_2-like component can lead to the better oxidation kinetics and a lower charge voltage.[148] Second, the charge voltage is closely related to the Li_2O_2 morphology. Even with the same structure, due to the low electrical conductivity of Li_2O_2,[141] small product particles have larger interfaces and allow better contact between Li_2O_2 and electrolyte/electrode, facilitating electron transport and leading to the low average charge voltage plateaus.[152] Third, the kinetics of oxidizing bulk Li_2O_2 is sensitive to rates and catalysts,[145] and the catalyst does not act conventionally to lower the activation energy through electron transfer, but acts as a promoter to enhance surface transport of Li_xO_2 species by reducing their binding energy in both the forward and reverse electrochemical processes.[153]

Although the detailed OER mechanism is unrevealed, a general descriptor of the OER activity is important for the selection of oxygen electrode materials. In alkaline media where

the OER is the reverse reaction as expressed in Equation 2, Shao-Horn *et al.* found that the specific OER activities of perovskite oxides exhibit a volcano shape as a function of the e_g-filling of surface B site cations, as shown in **Figure 6a**.[154] They proposed that the e_g-filling of surface transition metal cations can greatly influence the binding of OER intermediates to the oxide surface and thus the OER activity. For the right branch of the volcano, the rate-determining step is the formation of the O−O bond in OOH adsorbate on B-site ions, whereas for the left branch the deprotonation of the oxyhydroxide group to form peroxide ions may be rate-limiting. Thus, having the e_g-filling close to unity leads to the highest OER activity, such as $Ba_{0.5}Sr_{0.5}Co_{0.8}Fe_{0.2}O_{3-\delta}$ (BSCF, $e_g \approx 1.2$) reported by Shao and Haile.[155] Based on this perovskite oxide, Jung *et al.* distributed $LaCoO_{3-\delta}$ cobaltite particles on its surface to form a novel structured $La_{0.3}(Ba_{0.5}Sr_{0.5})_{0.7}Co_{0.8}Fe_{0.2}O_{3-\delta}$.[156] In this structure, 10 nm-size rhombohedral $LaCoO_{3-\delta}$ nanoparticles are distributed on the grain surface of cubic BSCF, forming flowerly particles. The resulting perovskite oxide featured with an increased surface area exhibit not only OER but also ORR activities that can be comparable to and even better than those of state-of-the-art noble metal oxides.

With the successful prediction of OER activities in alkaline solutions, Shao-Horn *et al.* further measured the activities of various perovskite oxides for Li_2O_2 electrochemical oxidation in a non-aqueous electrolyte (0.1 M $LiClO_4$/DME).[157] However, they found that the kinetics of Li_2O_2 oxidation by $LaNiO_3$, $LaMnO_{3+\delta}$, and $LaFeO_3$ exhibits similar activities to VC, as shown in Figure 6b. In contrast, the mass-specific net oxidation currents of $LaCrO_3$ and BSCF are greater than that of VC by one order of magnitude (Figure 6c). The X-ray diffraction (XRD) and scanning electron microscope (SEM) analyses showed that Li_2O_2 was removed largely from these electrodes upon potentiostatic charging at 4.0 V_{Li}, so that the current curves suggested the activities of the perovskite oxides toward OER in LOBs rather than the decomposition of electrolyte.[158-163] When considering the e_g-filling of the studied

perovskite oxides, as shown in Figure 6d, no clear trend in the activities against Li_2O_2 oxidation ($LaCrO_3$ >> BSCF > $LaNiO_3$ ≈ $LaMnO_{3+\delta}$ ≈ $LaFeO_3$) versus the e_g-filling can be found, which is on the contrary to the clear volcano trend for oxygen evolution kinetics during water oxidation in 0.1 M KOH (BSCF >> $LaNiO_3$ ≈ $LaFeO_3$ >> $LaMnO_{3+\delta}$ ≈ $LaCrO_3$) shown in Figure 6a. Strikingly, the least active perovskite oxide for oxygen evolution in alkaline solution, $LaCrO_3$, shows the most active for Li_2O_2 oxidation. Following this result, they further found that the activity of Cr nanoparticle is ~50 times higher than VC. It is proposed that in $LaCrO_3$, the ability of Cr compounds to accommodate mixed valence states of Cr^{3+} and Cr^{6+} ions on the surfaces can promote Li_2O_2 oxidation kinetics by facilitating electron removal necessary to carry out the oxidation step of Li_2O_2 to LiO_2 (Equation 8). As a result, Cr-based materials may be the effective catalysts.[164-166]

The above result shows the different reaction mechanisms for perovskite oxides from H_2O oxidation to Li_2O_2 oxidation. It is worth noting that the kinetics of OER in LOBs is not only determined by the catalyst itself, but also affected by how Li_2O_2 is produced, which is closely related to the ORR process.[46,75] Hence, the OER and ORR processes in LOBs are entangled and both should be considered when studying the activities of perovskite oxides.

2.3. Design principle

From the above discussion, due to the unique oxygen electrochemistry in LOBs, a rational design principle for electrode materials with high activities is highly challenging. The DFT calculation, a fast and effective method bypasses experimental cost and time, has been used in the initial design of transition-metal oxides for ORR and OER. Cho *et al.* provided an insight into the catalytic mechanism of ORR through DFT calculations of α-MnO_2 surfaces.[167] They found that the oxygen sites on the surface play a more important role than the exposed metal sites, since lithium ions from electrolytes interact with the surface oxygen sites and form surface lithium sites, facilitating further growth of Li_2O_2. In addition, the reduced size and homogeneous distribution of Li_2O_2 make the decomposition during OER much easier. Hence,

the significant determinant for the catalytic activity of metal oxides is the surface oxygen density on their exposed facet. To reveal the catalytic mechanism of transition-metal oxides for OER, Liu *et al.* studied the decomposition reaction of Li_2O_2 supported on Co_3O_4 surfaces.[168] The result indicated that P-type doping of Co_3O_4 (111) exhibits a good catalytic effect in decreasing both charging overpotential and O_2 desorption barrier. The ionization potential of doped transition-metal is thus determined to be an important parameter to regulate the catalytic activity of metal oxides. They further demonstrated that the O_2 evolution and lithium ion desorption energies show linear and volcano relationships with surface acidity of catalysts, respectively. Thus, certain materials with an appropriate surface acidity can achieve high OER activities.[169]

As LiO_2 is a key intermediate in both ORR (Equation 4) and OER (Equation 8), Han *et al.* calculated the LiO_2 adsorption energy as a descriptor on $LaB_{1-x}B'_xO_3$(001) (B, B' = Mn, Fe, Co, and Ni, x = 0.0, 0.5) to predict promising candidate catalysts.[170] They first investigated LiO_2 adsorption on $LaBO_3$(001), and found that the adsorption site preference of LiO_2 on the $LaMnO_3$ surface is almost identical for the other $LaBO_3$ perovskite surfaces. However, the trend in the adsorption energies on $LaBO_3$(001) follows the order of atomic number of the B-transition-metals (Mn, Fe, Co, Ni). When studying LiO_2 adsorption on $LaB_{0.5}B'_{0.5}O_3$(001), they found that the adsorption energy and site preference of LiO_2 on $LaB_{0.5}B'_{0.5}O_3$ surfaces are not dependent on those characteristics of the undoped $LaBO_3$ or $LaB'O_3$ surfaces, implying that it is hard to minutely tune the activity by doping or mixing of different metals in perovskite oxides. To understand the adsorption phenomenon in detail, the charge density difference was further analyzed. The results in **Figure 7a** indicate that O_t has the most negative charge state and O_b and Li have relatively lower negative charge states after adsorption. Moreover, the total charge density differences of adsorbed LiO_2 always have negative values which are related to the adsorption energies of LiO_2. Figure 7b shows the adsorption energies as a function of the changes in electron density on the ten bare or doped

perovskite surfaces, suggesting that the adsorption strength of the LiO_2 molecule is mainly determined by electron charge transfer between the adsorbate and the perovskite oxide surface. Their results showed that $LaMnO_3$, $LaMn_{0.5}Fe_{0.5}O_3$, or $LaFeO_3$ are promising candidate catalysts owing to their weak LiO_2 adsorption.

Although DFT calculations have been identified to predict trends in activity of perovskite oxides, for LOBs where the solid Li_2O_2 forms as the discharge product, the microstructure of perovskite oxides also has a significant role in the discharge performance. Besides, the ORR and OER kinetics are tightly correlated, so that how Li_2O_2 is formed should be considered in analyzing the OER process. Therefore, the design principles of perovskite oxides for LOBs may be totally different from that for aqueous solutions and new approaches are required.

3. Perovskite oxides as electrode materials

In the above section, we introduced the oxygen electrochemistry and the proposed mechanisms on the surfaces of perovskite oxides in LOBs. In this section, we summarize the perovskite oxides that have been applied as the oxygen electrode materials and the corresponding performance. Since the discharge product Li_2O_2 is in the solid state, which not only affects the reaction kinetics by covering the active sites, but also influences the transport kinetics. The structure of the electrode material, therefore, plays more significant role in the electrochemical performance. For this reason, we divide this section into three main parts in terms of the perovskite oxide structures used in the battery. We first review various perovskite oxide nanoparticles, including the direct use as catalysts and the investigations about the effects of geometries and cations. The hierarchical porous structure is followed, with highlighting the structural merits in improving the battery performance. To avoid the instabilities of carbon and binder and increase the discharge capacity, an integrated electrode made of perovskite oxide is also introduced.

3.1. Nanoparticles

The perovskite oxide nanoparticles that have been used as catalysts in the oxygen electrodes are summarized in Table 1. Xu *et al.* synthesized $LaNiO_3$ nanoparticles with a grain size far less than 100 nm and a surface area of 22.7 m^2 g^{-1}, as the morphology shown in **Figure 8a**.[171] When evaluating the electrocatalytic activity of the as-synthesized $LaNiO_3$ through cyclic voltammogram (CV), as shown in Figure 8b, the $LaNiO_3$/Super P (SP) electrode at 18 wt% loading of $LaNiO_3$ presented a lower anodic onset potential, a higher cathodic peak voltage, and larger reduction and oxidation currents than those of the SP electrode, demonstrating the efficient catalytic activities toward ORR and OER. The discharge and charge voltage profiles of a battery with this $LaNiO_3$/Super P electrode is illustrated in Figure 8c. It presented a voltage gap of 878 mV, which is 706 mV lower than that of the SP electrode. In addition, the $LaNiO_3$/SP electrode exhibited superior cyclability up to more than 155 cycles and a more stable discharge voltage (>2.51 V), far greater than those of the SP electrode (Figure 8d), indicating the high intrinsic activity of $LaNiO_3$. $La_{0.6}Sr_{0.4}Co_{0.2}Fe_{0.8}O_3$ (LSCF), as a typical cathode material for SOFCs owing to its high oxygen surface exchange coefficient for fast kinetics at the gas/cathode interface, was also applied in non-aqueous LOBs.[133] The study revealed that the formation and decomposition of Li_2O_2 can be effectively promoted by the introduction of LSCF nanoparticles. As a result, batteries with LSCF catalyst can deliver a discharge capacity of 20039 mAh g^{-1} and improve the cycle stability to 17 cycles. In addition to lanthanum (La)-based perovskite oxides, $Ba_{0.9}Co_{0.7}Fe_{0.2}Nb_{0.1}O_{3-\delta}$ (BCFN) perovskite oxide, which exhibits a high oxygen mobility and surface oxygen exchange reaction rate, was tested in LOBs by Song *et al.*[172] They found that adding 20% BCFN could effectively reduce the polarization and achieve better bi-functional activities for the electrochemical reactions, especially for the OER. The charge polarization was therefore significantly reduced and alleviated the formation of side products. Even though the improved battery performance can be obtained through the direct use of perovskite oxide nanoparticles, investigating the factors that affect the electrochemical activities is crucial for material selection and optimization.

3.1.1. Effect of particle size and defect

For non-aqueous LOBs, the electrode surface will be gradually covered with an increase in the capacity due to the formation of solid Li_2O_2. Consequently, a large surface area of the electrode material is important for a large capacity. Fu *et al.* fabricated the nano-sized $La_{0.8}Sr_{0.2}MnO_3$ with a surface area of 32 m^2 g^{-1} and compared with the prinstine one (1 m^2 g^{-1}).[173] The nano-sized perovskite oxide delivered a higher voltage plateau and a larger capacity because of the greatly improved surface area. The mechanical process by ball milling (BM) is one of the attractive techniques in preparing perovskite oxides, which can reduce the particle sizes.[174] Nahm *et al.* investigated the effects of BM on the structural and electrochemical characteristics of $La_{0.6}Sr_{0.4}CoO_{3-\delta}$ (LSC).[175] As the BM time increased, the particle size decreased and the surface area increased, as illustrated in Table 1. Besides, it is found that crystal defects and dislocations were formed through ball milling, resulting in the structural change from single to polycrystalline structures. Since boundaries, defects and dislocations are considered to be active sites of electrocatalysis,[176] the better ORR and OER activities in alkaline solution were observed from the ball milled LSC, which might be due to the reduced particle size and the increased defect density.[177] When applying as the oxygen electrode catalyst in a LOB, the 24-hour BM LSC performed the best discharge and charge performance, with 3256 mAh g^{-1} for discharge and a voltage gap of 0.85 V at a capacity of 1100 mAh g^{-1}, as well as the longest cycle life up to 43 cycles. Their results indicated that the increased surface area and crystal defect density can promote the reaction kinetics with more number of active sites on the surface and aid the formation and decomposition of the discharge product, improving the catalytic activities. The role of vacancies and defects of metal oxides in LOBs was also investigated by Nazar *et al.* through treating $Na_{0.44}MnO_2$ nanowires in nitric acid to induce controllable defect formation.[178] The high defect concentration could result in a doubling of the reversible energy storage capacity and lower overpotentials for oxygen evolution. The greater ORR activity may come from the more

accessibility of O_2 to the active binding sites and the pathway for O_2 to the interior of the nanowire along its entire exterior length; the improved OER activity may be attributed to the structural defects and microstrains that facilitate the destabilization of Li_2O_2 upon charge.

3.1.2. Effect of A-site substitution

In addition to changing the surface area and crystal defect through physical approaches, doping in A and/or B site is another strategy to improve the catalytic activities. In alkaline solutions, the effects of the A-site substitution on the ORR/OER activities have been investigated, which may be attributed to the differences in crystal structures, ionic radii/binding energies, and electrical conductivities.[100] Although some La-based perovskite oxides with partial A-site substitution (e.g., $La_{0.6}Sr_{0.4}CoO_{3-\delta}$[175]) have been applied in non-aquoeus LOBs, few studies have been conducted to investigate the effects of A-site cation on the electrochemical performance. Francia *et al.* compared Pb, Ba and Sr in the form of $La_{0.65}X_{0.35}MnO_3$ (X = Pb, Ba, Sr) as electrode materials in terms of discharge capacity, charge overpotential, and cycle life.[179] At the same current density, the $La_{0.65}Pb_{0.35}MnO_3$-based electrode delived a capacity of 7211 mAh g^{-1}, higher than that of $La_{0.65}Sr_{0.35}MnO_3$ (6760 mAh g^{-1}) and $La_{0.65}Ba_{0.35}MnO_3$ (6205 mAh g^{-1}). However, the $La_{0.65}Sr_{0.35}MnO_3$ electrode could significantly decrease the charge overpotential. The reason might be that large Li_2O_2 toroids were formed in $La_{0.65}Pb_{0.35}MnO_3$ and $La_{0.65}Ba_{0.35}MnO_3$ electrodes, while $La_{0.65}Sr_{0.35}MnO_3$ electrode promoted the formation of smaller aggregates of Li_2O_2, facilitating the charge process. When considering the cycle performance, the battery with $La_{0.65}Pb_{0.35}MnO_3$ electrode showed about 35 cycles with a coulombic efficiency ranging from 95 to 97%, higher than the other two electrodes. Hence, no clear trends could be obtained from the A-site substitution in the non-aqueous system, and further intensively studies are needed.

3.1.3. Effect of B-site substitution

B-site cations have also been shown to strongly affect the electrocatalytic activities,[100] because of the possible formation of redox couples near the oxygen reduction region and the tunable bond strength of B−OH.[89] To understand the B-site substitution on the electrochemical performance of LOBs, a detailed investigation of different elements doping is needed.

Du *et al.* investigated the electrochemical performance of Mg-doped perovskite oxides $LaNi_{1-x}Mg_xO_3$.[180] In the alkilne solution, the increased Ni^{3+}/Ni^{2+} ratio and absorbed hydroxyl on the surface of Mg substituted perovskite oxides strongly increase oxygen mobility at a lower scale, and thus improve the ORR kinetics. In addition, greater covalency between Ni and oxygen in $LaNi_{0.85}Mg_{0.15}O_3$ promotes the charge transfer between surface cations and adsorbates, leading to higher OER activity. As a result, the battery with $LaNi_{0.85}Mg_{0.15}O_3$ electrode exhibited a discharge capacity twice higher than that with the $LaNiO_3$ electrode. Due to the better thermal stability with Mn in the B site than that with Co, Liu *et al.* doped Mn in the B site to partially substitute for Co in $La_{0.6}Sr_{0.4}CoO_3$.[181] They found that with an increase in the content of Mn, the surface area and grain size were hardly changed, whereas the electrochemical performance was improved. In a 1.0 M LITFSI/tetramethylene sulfone electrolyte, a battery with the $La_{0.6}Sr_{0.4}Co_{0.9}Mn_{0.1}O_3$ catalyst showed the highest discharge capacity of 3107 mAh g^{-1} at a current density of 200 mA g^{-1}, and was maintained a fixed discharge capacity of 500 mAh g^{-1} for 50 times with 3.28% voltage loss. Hence, Mn in the B site could make this perovskite oxide more stable and excellent catalytic activity. Because Ni holds the lowest oxygen vacancy formation energy, the influence of doping Ni has also been investigated.[182-184] For $La_{0.8}Sr_{0.2}MnO_3$, which has been reported among the leading perovskite-type catalysts for ORR, is suffered from an intrinsically low activity for OER due to the weak covalency of Mn−O bond and the lack of transition-metal ions. To address this issue, Wang *et al.* doped Ni in Mn site.[183] They found that an increase in the content of doped Ni led to a decreased particle size, and as a result $La_{0.8}Sr_{0.2}Mn_{0.6}Ni_{0.4}O_3$ showed the

largest surface area (14.41 $m^2 g^{-1}$) that nearly doubled that of the undoped one (8.69 $m^2 g^{-1}$). The capacity of $La_{0.8}Sr_{0.2}Mn_{0.6}Ni_{0.4}O_3$ is 5364 mAh g_{carbon}^{-1}, higher than that of $La_{0.8}Sr_{0.2}MnO_3$ (4408 mAh g_{carbon}^{-1}), which is attributed to the abundant oxygen vacancies that can efficiently catalyze the formation of Li_2O_2 in the discharge process. Moreover, the charge voltage plateau of $La_{0.8}Sr_{0.2}Mn_{0.6}Ni_{0.4}O_3$ is approximately 180 mV lower than that of $La_{0.8}Sr_{0.2}MnO_3$, which may correlate with the existence of trivalent Ni on the surface, resulting in the interaction between Li_2O_2 or LiO_2 and oxygen vacancies to easily release the electrons and lithium ions. The improved ORR and OER activities made $La_{0.8}Sr_{0.2}Mn_{0.6}Ni_{0.4}O_3$ achieve a cycle number up to 79 at a fixed capacity of 500 mAh g_{carbon}^{-1}, proving that the abundant oxygen vacancies could contribute to maintaining a stable performance.

Apart from perovskite oxides, other types of perovskite-based oxides have also been applied as the catalysts in LOBs. Lee *et al.* tested the electrochemical activity of a layered perovskite oxide, $La_{1.7}Ca_{0.3}Ni_{0.75}Cu_{0.25}O_4$ (LCNC), in the oxidation of solid Li_2O_2.[185] They demonstrated that compared with the perovskite oxide $La_{0.8}Sr_{0.2}MnO_3$, the LCNC-containing electrode showed a lower charge potential. In addition, the battery with the LCNC-containing electrode delivered higher capacities and exhibited improved capacity retention during cycling compared to that with the catalyst-free electrode. Yuan *et al.* reported the application of the double perovskite oxide $Sr_2CrMoO_{6-\delta}$, which exhibited a higher discharge capacity, lower overpotentials, better rate capability and cycle performance, and higher reversibility than those of Super P.[186] The improved performance may be attributed to that the double perovskite oxide has a much higher oxygen and electron transport ability than the general perovskite oxides.

Although the effects of different factors on the electrochemical performance of perovskite oxide nanoparticles have been investigated, it is worth noting that the studies are based on the specific perovskite oxide rather than a general benchmark (e.g., $LaNiO_3$),

making it hard to do comprehensive comparisons. In addition, as listed in Table 1, some battery performance was tested with carbonate-based solvents which were unstable during discharge and charge, leading to the difficulty in estimating the real electrochemical activities of applied perovskite oxides.[18-21] Hence, a systematical investigation based on a benchmarked perovskite oxide, and carried out in a stable non-aquoeus electrolyte, is in a great demand.

3.2. Hierarchical porous structure

The highly catalytic activities of perovskite oxide nanoparticles make them the promising catalysts in LOBs. However, as listed in Table 1, due to their similar scales (<100 nm) to those of carbon nanoparticles (40 nm),[133] similar pore sizes to those formed by carbon nanoparticles will be formed after the electrode fabrication. Because the solid product deposites in the oxygen electrode and changes its porous structure, affecting the triple-phase boundaries,[187] the pore size is therefore a crucial factor for the battery performance. It is found that in the ordered meso- and macroporous carbon materials, the discharge capacity is directly correlated with the pore size.[111] For graphene-based materials, two important factors are responsible for the improved performance,[188] including the morphology of graphene in which numerous large tunnels facilitate a continuous oxygen flow and the small pores provide triple-phase boundaries for the oxygen reduction.[106] For catalyst materials, in addition to abundant active sites, the mesopores associated with high specific surface area and large pore volume are significant,[189] which not only facilitate the access of reactants to active sites and favor the mass transport of intermediate species, but also lead to enhanced electron delivery to active sites due to the continuous framework structure.[190] Hence, desirable electrode architectures should incorporate hierarchical pores from micro- to meso- and macroscale to achieve effective oxygen diffusion, liquid electrolyte wetting and solid product accommodation.[191]

Chen *et al.* reported the usage of interconnected porous perovskite $CaMnO_3$ as the catalyst in LOBs.[194] As shown in **Figure 9a**, the macroporous structure is formed through $CaMnO_3$ nanoparticles with an average diameter of 57 nm, resulting in a high surface area of 32.0 $m^2\ g^{-1}$. At a current density of 50 mAh g_{carbon}^{-1}, as shown in Figure 9b, the $CaMnO_3$-based battery displayed a voltage gap of 0.98 V, lower than that of carbon-based one (1.60 V). With a fixed capacity of 500 mAh g_{carbon}^{-1}, the $CaMnO_3$ electrode attained good cyclability (>80 cycles) with a stable discharge voltage (>2.35 V), whereas the carbon-only electrode could merely sustain less than 25 cycles (Figure 9c). The improved performance of interconnected porous $CaMnO_3$ is attributed to the high electrocatalytic activity and the porous structure for mass transport and product accumulation. To further demonstrate the advantages of hierarchical porous structure, Zhang *et al.* prepared three-dimensionally ordered macroporous $LaFeO_3$ (3DOM-LFO), and compared the performance with LFO nanoparticles (NP-LFO).[195] As shown in Figure 9d, the interconnected inorganic walls created a "honeycomb" pore structure in three dimensions. The open and interconnected 3DOM structure gives a surface area up to 29.3 $m^2\ g^{-1}$, much higher than that of NP structure (1.4 $m^2\ g^{-1}$). The electrochemical performance was tested in a battery as shown in Figure 9e. Although the discharge voltage of 3DOM-LFO/KB electrode is only slightly higher than that of NP-LFO/KB by about 20 mV and KB by about 30 mV, its charge voltage is much lower than that with NP-LFO/KB electrode by 150 mV and KB by 250 mV, indicating the enhanced ORR and OER kinetics. At the same current density, the battery with 3DOM-LFO electrode delivered a capacity of 11,738 mAh g^{-1} during the initial discharge, higher than that with NP-LFO electrode (~11,000 mAh g^{-1}). Moreover, at a fixed capacity of 1000 mAh g_{carbon}^{-1}, a battery with the 3DOM-LFO electrode exhibited almost no degradation even after 124 cycles (Figure 9f), much higher than that with NP-LFO (75 cycles). Similarly, Nahm *et al.* fabricated three-dimensionally ordered macroporous perovskite $La_{0.6}Sr_{0.4}CoO_{3-\delta}$ (3DOM-LSC), and

demonstrated a higher discharge capacity and longer cycle life than those of LSC nanoparticles.[196]

In addition to the macroporous structure formed through the interconnection of perovskite oxide nanoparticles, various hierarchical-structured perovskite oxides with unique morphologies have been fabricated and applied in LOBs, including nanowire,[132] nanotube,[197-199] nanorode,[200] and nanocube,[201] as summarized in Table 2 and **Figure 10**. Compared with nanoparticles, the structural merit has a significant effect on the battery performance. For example, Zhang *et al.* synthesized the porous tubular structured $La_{0.75}Sr_{0.25}MnO_3$ nanotubes (PNT-LSM) and used them as the electrode catalysts in LOBs.[197] For the PNT-LSM/KB electrode, the porous nanotubes are dispersed disorderly in KB carbon, making the electrode loose and porous and providing sufficient space for the discharge product deposition (**Figure 11a**). In addition, the porous tubular LSM nanotubes offer more abundant oxygen and electrolyte transportation paths in the electrode, helping to get uniform oxygen and electrolyte distribution inside the electrode, as schematically shown in Figure 11b. In contrast, the conventional KB electrode shown in Figure 11d is made of tightly stacked carbon particles, leading to a low porosity, which would easily block oxygen molecules and decrease the electrochemically available surface area (Figure 11e). With the aid of PNT-LSM catalysts, the battery obtained a much improved specific capacity and rate capability. In the voltage range of 2.2−4.4 V, a battery exhibited rather stable specific capacities above 9,000–11,000 mAh g^{-1} for five cycles (Figure 11c). On the contrary, the capacity of the KB electrode was only ~8,200 mAh g^{-1} in the initial discharge, but decreased dramatically to 2,313 mAh g^{-1} after five cycles, as shown in Figure 11f. It is worth noting that the battery's cycle performance is usually tested in a capacity-limited condition,[202] because the deposition and decomposition of solid Li_2O_2 in LOBs may cause blockage and deformation of the air electrode at a deep discharge.[203] To date, limited electrode materials have been reported in the literature that can run the cycle performance in a full discharge-charge (potential cut-off)

condition, such as porous Au,[42] TiC,[117] and RuO_2.[73,204] Here the electrode with PNT-LSM successfully enabled the cycle performance in a potential cut-off condition, with the charge capacity closed to the discharge capacity after each cycle and a coulombic efficiency of approximately 100%. The better results might be attributed to the unique properties of the electrode with porous, open, and tubular PNT-LSM catalyst, facilitating the formation and decomposition of the discharge product and improving the reversibility.

In addition to PNT-LSM, other perovskite oxides can also demonstrate the good cycle performance in a full discharge-charge condition, such as the 3D ordered macroporous $LaFeO_3$,[196] $La_{0.8}Sr_{0.2}MnO_3$ nanorods,[200] and $La_{0.5}Sr_{0.5}CoO_{3-\delta}$ nanotubes,[198] as summarized in Table 2. In summary, the hierarchical porous structured perovskite oxides have the following advantages: i) high surface areas with mesopores and macropores can offer a large electrode-electrolyte contact area to ensure sufficient active sites for electrochemical reactions and more spaces for solid product storage; ii) short diffusion distances for species (e.g., O_2 and Li^+) can improve the mass transport rate; and iii) direct current pathways can facilitate electron transport. When employing in the oxygen electrode, all these favorable advantages benefit the electrochemical performance of LOBs.

3.3. Integrated electrode

The above-mentioned perovskite oxides are used as the catalysts with the combination of a carbon matrix, a binder, and a current collector/substrate (e.g., Ni foam, carbon paper) to form the oxygen electrode. However, these additives increase the electrode weight, leading to a low obtainable discharge capacity, especially when taking the heavy weight of the current collector/substrate into consideration.[205] In addition, it has been shown that both the highly oxidizing environment and the discharge product (Li_2O_2) can lead to the decomposition of the carbon[206,207] and the binder (e.g., PVDF)[208] to form side products. These irreversible side products passivate the electrode, leading to rapid polarization in charge as well as capacity fading on cycling.

To address these issues, Wei *et al.* proposed an integrated electrode made of pure $LaNiO_3$ without the need of a carbon matrix and a current collector/substrate.[209] The porous electrode was made by sintering the $LaNiO_3$ powder and the pore-former, and the microstructures were optimized through adjusting the weight ratio of pore-former. As shown in **Figure 12a**, this integrated electrode allows the formation of nanosized pores on the wall of microsized pores, facilitating the transport of both oxygen and lithium ions. Additionally, $LaNiO_3$ supplies enough electrical conductivity to support electron transport. Moreover, all surfaces of the porous structure are catalytically active for electrochemical reactions. A battery with this electrode delivered a voltage plateau of 2.85V with a discharge capacity of 1.064 mAh cm^{-2}. At a fixed capacity of 0.3 mAh cm^{-2}, the battery was also stable for cycling. After 34 cycles, the oxygen electrode was reassembled into a battery with a fresh lithium electrode, a glass-fiber separator, and an electrolyte, and delivered almost the same voltage profiles as the initial one (Figure 12b). To further confirm the stability of the $LaNiO_3$ electrode, the composition of the discharge products and electrode after different numbers of cycles were investigated by X-ray photoelectron spectroscopy (XPS), as shown in Figure 12c and 12d. After the 34^{th} discharge, the peak intensity of Li-based byproducts is stronger than that after the 5^{th} discharge, indicating that the decayed performance was attributed to the accumulation of byproducts on the electrode surface. Correspondly, the Ni 2p peak decreased significantly after the 34^{th} discharge. For the reassembled battery, a significant decrease of the peak intensity for Li-based byproducts can be found, and the initial state of Ni was recovered.

Although various kinds of perovskite oxides with different microstructures have been applied in LOBs, and some good performance has been reported, there still exist some remaining issues as summarized below: i) The unknown stability. Studies of carbon show that carbon can react with discharge products (e.g. Li_2O_2) and also promote the decomposition of electrolytes, resulting in the formation of irreversible side products (e.g. Li_2CO_3) covering the active sites and leading to the performance degradation.[206,207] To avoid the side reaction from

carbon, several approaches have been developed, including passivating the defects by a protective Al_2O_3 coating,[210] fabricating a catalyst shell on the carbon surface to prevent the direct contact with Li_2O_2 and electrolyte,[211] and using the interaction between the ionic solvate and active sites of carbon to deactivate the surface.[212] Although carbon is usually accompanied with perovskite oxides in the air electrode, the above-mentioned methods to suppress the side reactions have not been reported. In addition, the stabilities of perovskite oxides in the oxidizing environment and towards different kinds of non-aqueous electrolytes, however, have not been systematically investigated yet. Especially for those perovskite oxides with abundant oxygen vacancies, whether the active surfaces can be maintained after long-term operation requires further estimation. Moreover, the synergetic effects of carbon and perovskite oxides on the stability, if exist, should require great concerns. ii) The low specific surface area. Although an improved surface area has been obtained through decreasing the particle size or designing the microstructure, the value is still low (<100 $m^2\ g^{-1}$). Owing to the formation of solid products, the surface area will be further decreased during discharge, limiting the battery performance, especially at high current densities. Hence, developing novel fabrication methods to achieve high specific surface areas is in great need. Through precisely controlling the inorganic to organic precursor ratio in the gel and its decomposition temperature, metallic Magnéli phase Ti_4O_7 with a crystallite size between 10–20 nm and a specific surface area as high as 180 $m^2\ g^{-1}$ was successfully synthesized.[213] Recently, a new approach for synthesizing ultrafine metal oxide nanoparticles has been reported,[214] which used an electrochemical prelithiation process to reduce the size of $NiCo_2O_4$ particles from 20−30 nm to a uniformly distributed domain of ~2 nm. More importantly, the prelithiated $NiCo_2O_4$ nanowires with ultrafine nanoparticles are highly stable during long-term cycles in both morphology and particle size, maintaining an excellent catalytic effect to ORR and OER. This unique approach may also be used to form ultrafine nanoparticles of perovskite oxides to further improve the surface area. iii) The difficulty in the morphological control. Different

hierarchical structured perovskite oxides have been fabricated, with which the battery performance has been enhanced. However, during cycling the formation and decomposition of solid Li_2O_2 will cause the expansion and shrinkage of the void volumes in the oxygen electrode, breaking down the well-degined morphology. To achieve long cycle life, the hierarchical structured perovskite oxide with a stable morphology and long-term mechanical strength is essential.

4. Perovskite oxide-based composites

In the above-mentioned works, perovskite oxides were synthesized alone and used as electrode materials. Although some impressive results have been achieved, the drawbacks of perovskite oxides, such as the low surface areas and high transport resistance of aggregated nanoparticles, hinder the further improvement of electrochemical performance. An effective strategy to address these issues is to combine perovskite oxides with other materials to form composites with improved physical and chemical properties. In the following paragraphs, we discuss the perovskite oxide-based composite materials used in LOBs with highlighting the merits come from material incorporation and structural assembly.

4.1. Material incorporation

As illustrated in Table 1 and 2, the low specific surface area is one drawback of perovskite oxides. To increase the reaction sites for oxygen reduction, Yuasa *et al.* dispersed $LaMn_{0.6}Fe_{0.4}O_3$ nanoparticles on the carbon powder support through a reverse homogeneous precipitation method.[215] However, due to the instability of carbonate-based electrolytes in their tests, the real activities for the carbon-supported perovskite oxide need further estimations.[216] Based on the similar material, $LaFe_{0.5}Mn_{0.5}O_3$, Ce is chosen to dope in with different atomic ratios,[217] because it is reported that through the replacement of inert La cation by active Ce, not only oxygen capture can be enhanced,[218] but also conductivity can be increased.[219] However, the results showed that Ce has a very low solubility in $LaFe_{0.5}Mn_{0.5}O_3$ lattices, and the Ce-incorporated samples are mainly $LaFe_{0.5}Mn_{0.5}O_3$-CeO_2

composite instead of single-phase $La_{1-x}Ce_xFe_{0.5}Mn_{0.5}O_3$. When testing the discharge performance of the composite in a 0.1 M $LiClO_4$/DMSO electrolyte, the capacity followed the ranking of Ce/(La+Ce) = 0.05 > Ce/(La+Ce) = 0.1 > Ce/(La+Ce) = 0.5 > Ce/(La+Ce) = 0. The enhanced capacity may be attributed to the enhanced capability of releasing oxygen, faster charge transfer, and better electrocatalytic activity caused by a small amount of CeO_2. However, higher Ce concentration results in a large quantity of the more insulating CeO_2 in the composite, resulting in a decreased capacity.

4.2. Structure assembly

Although the incorporations of Ce can improve the performance of pristine perovskite oxides in LOBs, the aggregation of composite particles with high oxygen and lithium ion transport resistance is one main barrier toward high performance. A strategy to address this issue is to assemble perovskite oxides with other materials to achieve a porous structure with improved transport kinetics.

Lee *et al.* compounded $LaCoO_3$ (LCO) nanoparticle (NP) with different weight ratio of reduced graphene oxide (rGO) to form the LCO-rGO composites, as schemed in **Figure 13a**.[220] They found the LCO NP aggregates were completely surrounded by rGO nanosheets with 10.5 wt% of rGO (LCO-rGO-10.5), but were partially exposed in the composite with 7.5 wt% of rGO (LCO-rGO-7.5). In a 1.0 M $LiCF_3SO_3$/TEGDME electrolyte, the batteries with the composite performed higher capacities, smaller voltage gaps, and longer cycle lives than those with pristine rGO or neat LCO NPs. Between the two composites, LCO-rGO-10.5 delivered a higher capacity of 5197 mAh g^{-1}, but the LCO-rGO-7.5 showed a longer cycle life up to 195 cycles. The performance improvement could be attributed to an increase in extrinsic conductivity due to the presence of rGO nanosheets and the alleviation of LCO NP aggregation and rGO nanosheet restacking due to the synergy effects. The free volumes created are also useful for storing solid Li_2O_2 and facilitating the transport of lithium ions and oxygen. Yang *et al.* coated thin meso-$La_{0.8}Sr_{0.2}MnO$ layers throughout a graphene foam (G-

foam) to form graphene/meso-$La_{0.8}Sr_{0.2}MnO$ (G/meso-LaSrMnO) sandwich-like nanosheets, as schemed in Figure 13b.[221] As graphene served as a porous flexible template and conductive network, a macroscopic 3D hierarchical architectures was fabricated. In this electrode, the macropore between nanosheets facilitates transport kinetics, the mesopore provides a large surface area for electrolyte immersion and Li_2O_2 deposition, the perovskite oxide increases reaction kinetics, and the graphene serves as a conductive network for electron transport. In a battery with a 1.0 M LITFSI/TEGDME electrolyte, the specific capacity reaches 6515 $mAh \cdot g^{-1}$ based on the total weight of the composite foam, corresponding to a capacity of 21470 $mAh \cdot g^{-1}$ with respect to catalyst loading and 9044 $mAh \cdot mL^{-1}$ with respect to the pore volume of the electrode. At a high current density of 500 $mA \cdot g^{-1}$, the discharge capacity of the G/meso-LaSrMnO electrode kept at 2500−4500 $mAh \cdot g^{-1}$ even at the 10 full charge and discharge, with a high capacity retention of 55%, showing a good cycling stability.

In addition to the combination of perovskite oxide nanoparticle and graphene, Kim *et al.* reported a structural assembly of low-dimensional electrode materials composed of 0D RuO_2 nanoparticles (NPs), 1D perovskite $LaMnO_3$ nanofibers (NFs), and 2D graphene nanosheets.[222] As schemed in **Figure 14a**, the $LaMnO_3$ NFs were first prepared through the electrospinning method, after which the oxide surfaces were decorated by RuO_2 NPs as co-catalysts. Then, the $RuO_2/LaMnO_3$ composite NFs were randomly laid onto both sides of non-oxidized graphene nanoflakes (GNFs), affording an alternative electron pathway and additional reaction sites. The TEM images of the GNF-$RuO_2/LaMnO_3$ NFs are shown in Figure 14b-14d, which clearly presented the assembled structure. Under a fixed capacity of 1000 mAh g^{-1}, as shown in Figure 14e, the KB electrode showed a huge voltage gap at around 2.0 V between the discharge and charge voltages, whereas the voltage gaps were lowered to 1.0 V for the GNF-$RuO_2/LaMnO_3$ NFs electrode. In addition, the cycle performance shown in Figure 14f demonstrated that the GNF-$RuO_2/LaMnO_3$ NFs electrode

exhibited the highest cycle life of over 320 cycles without severe voltage degradation. The outstanding performance might be attributed to the following reasons: i) $LaMnO_3$ NFs provide a rigid scaffold without burying into the carbon supports, preserving the reaction; ii) RuO_2 NPs on the $LaMnO_3$ NFs provide catalytic activities and electrical conductivity; and iii) widely spread GNFs support the RuO_2/$LaMnO_3$ NFs facilitate the charge transfer as well as ORR kinetics. Hence, the integration of various functional and multi-dimensional materials is a competitive way to achieve high performance.

In perovskite oxide-based composites, due to the additional materials with unique merits (e.g., surface area, electrical conductivity, microstructure), the performance of LOBs could be further improved. However, attentions should be paid to several aspects. First, the stabilities of the incorporated materials in the oxidizing environment and/or towards the electrolyte need to be noticed. Second, the results obtained through using perovskite oxide-based composite should be compared with both the perovskite oxide and the incorporated material to fully demonstrate the advantages of the composite. Third, as one advantage of perovskite oxides is the nobel-metal free, cost-effective materials should be chosen as the incorporated materials instead of noble ones.

5. Summary and outlook

The commercialization of non-aqueous lithium-oxygen batteries is hindered by a variety of technical hurdles, including low obtainable capacity, poor energy efficiency, and limited cycle life, most of which are closely related to the oxygen electrode. Among various electrode materials, Perovskite oxides are ideally suited since they have the most desirable properties: high electrical conductivities, good catalytic activities, and low-cost. In this article, we focus on the recent advances in the development of perovskite oxides as the electrode materials for non-aqueous lithium-oxygen batteries. The general challenge for perovskite oxides is the pursuit of large specific surface areas, high electrical conductivities, good catalytic activities,

and proper microstructures. To fully reveal the potential of perovskite oxides, several issues need to be addressed in the future research.

First, the oxygen electrochemistry mechanisms on the surface of perovskite oxides in non-aqueous lithium-oxygen batteries need to be clarified. The detailed oxygen reduction and evolution reaction mechanisms in aqueous solutions have been intensively investigated. However, such studies are rare in non-aqueous electrolytes. During the oxygen reduction reaction where the solid product Li_2O_2 is formed, the roles of perovskite oxide properties (e.g., oxygen vacancy) in the adsorption and reduction of oxygen and intermediate species are not clear. In addition, the activities of various kinds of perovskite oxides have not been systematically investigated yet. During the oxygen evolution reaction where solid Li_2O_2 needs to be electrochemically decomposed, it has been reported that the activities for some selected perovskite oxides are in contrast to those in alkaline solutions. However, a rational design principle for efficient perovskite oxides, from either molecular orbital theory or DFT calculations, is still absent. It is worth noting that different from the scenario in aqueous solutions, the oxygen evolution reaction is correlated to the oxygen reduction reaction in non-aqueous electrolytes, so that the synergy effects for both reduction and evolution reactions have to be considered. Therefore, a profound understanding of the electrochemical mechanisms is crucial for the proper selection of perovskite oxides, and the best approach to address this challenge should be a combination of advanced characterization techniques and theoretical analyses.

Second, much attention should be devoted to the microstructure of perovskite oxides used in the electrode. Due to the formation of solid Li_2O_2 with poor electrical conductivity, the triple-phase boundaries among oxygen, lithium ions, and electrons will be affected, resulting in a low discharge capacity and a high charge overpotential. To improve the battery performance, in addition to the high catalytic activities, the perovskite oxide should have structural merits to facilitate transport kinetics. Various kinds of unique structures (e.g.,

hierarchical macroporous/mesoporous structures) of perovskite oxides have been applied, with improved specific surface areas, short species diffusion distances, and direct current pathways. While the detailed microstructures should be tailored with taking the electrolyte properties and operating conditions into consideration. More importantly, the formation and decomposition of solid Li_2O_2 will cause the expansion and shrinkage of void volumes in the oxygen electrode during cycling, which may break down the designed morphology. The nanostructured perovskite oxide with a stable morphology and long-term mechanical strength is therefore essential for long cycle life.

Third, apart from using perovskite oxides along, developing perovskite oxide-based composites is significant. Through incorporation with other materials, not only the physi-chemical properties can be tuned, but also the structure can be tailored, so that both reaction and transport kinetics are improved. As the oxygen electrode stability has a crucial role in the cycle life, great care should be taken to the stabilities of the incorporated materials towards the electrolyte and in the oxidizing environment. In addition, the results by using perovskite oxide-based composites should be compared with both the perovskite oxide and the incorporated material to fully estimate the advantages got from the composite phases. Moreover, selecting cost-effective materials and developing facile fabrication methods to synthesize the composites are also important.

In summary, the mechanism investigation, structure design, and composite incorporation are significant and will be the central research topics of perovskite oxides in non-aqueous lithium-oxygen batteries. It is expected that with tremendous efforts, perovskite oxides can act as the promising electrode materials and deliver superior performance.

Acknowledgements

M. NI thanks the funding support from The Hong Kong Polytechnic University (G-YBJN), the RISUD (1-ZVEA), and the Environment Conservation Fund (ECF 54/2015).

Received: ((will be filled in by the editorial staff))
Revised: ((will be filled in by the editorial staff))
Published online: ((will be filled in by the editorial staff))

References

[1] E. J. Cairns, P. Albertus, *Annu. Rev. Chem. Biomol. Eng.* **2010**, *1*, 299.

[2] F. T. Wagner, B. Lakshmanan, M. F. Mathias, *J. Phys. Chem. Lett.* **2010**, *1*, 2204.

[3] Z. Wang, D. Xu, J. Xu, X. Zhang, *Chem. Soc. Rev.* **2014**, *43*, 7746.

[4] K. R. Yoon, J. Jung, I. Kim, *ChemNanoMat*. **2016**, *2*, 616.

[5] M. Wakihara, *Sci. Eng: R: Rep.* **2001**, *33*, 109.

[6] J. Lee, S. T. Kim, R. Cao, N. Choi, M. Liu, K. T. Lee, J. Cho, *Adv. Energy Mater*. **2011**, *1*, 34.

[7] G. Girishkumar, B. McCloskey, A. C. Luntz, S. Swanson, W. Wilcke, *J. Phys. Chem. Lett*. **2010**, *1*, 2193.

[8] P. G. Bruce, S. A. Freunberger, L. J. Hardwick, J. Tarascon, *Nat. Mater*. **2012**, *11*, 19.

[9] K. Abraham, Z. Jiang, *J. Electrochem. Soc.* **1996**, *143*, 1.

[10] R. Black, B. Adams, L. F. Nazar, *Adv. Energy Mater*. **2012**, *2*, 801.

[11] M. Park, H. Sun, H. Lee, J. Lee, J. Cho, *Adv. Energy Mater*. **2012**, *2*, 780.

[12] S. Meini, M. Piana, H. Beyer, J. Schwaemmlein, H. A. Gasteiger, *J. Electrochem. Soc.* **2012**, *159*, A2135.

[13] Y. Lu, B. M. Gallant, D. G. Kwabi, J. R. Harding, R. R. Mitchell, M. S. Whittingham, Y. Shao-Horn, *Energy Environ Sci*. **2013**, *6*, 750.

[14] K. G. Gallagher, S. Goebel, T. Greszler, M. Mathias, W. Oelerich, D. Eroglu, V. Srinivasan, *Energy Environ Sci*. **2014**, *7*, 1555.

[15] S. Meini, N. Tsiouvaras, K. U. Schwenke, M. Piana, H. Beyer, L. Lange, H. A. Gasteiger, *Phys. Chem. Chem. Phys*. **2013**, *15*, 11478.

[16] G. Wang, L. Huang, S. Liu, J. Xie, S. Zhang, P. Zhe, G. Cao, X. Zhao, *ACS Appl. Mater. Interfaces.* **2015**, *7*, 23876.

[17] D. Geng, N. Ding, T. S. A. Hor, S. W. Chien, Z. Liu, D. Wuu, X. Sun, Y. Zong, *Adv. Energy Mater*. **2016**, *6*, 1502164.

[18] J. Read, *J. Electrochem. Soc.* **2002**, *149*, A1190.

[19] W. Xu, J. Xiao, J. Zhang, D. Wang, J. Zhang, *J. Electrochem. Soc.* **2009**, *156*, A773.

[20] D. Zhang, Z. Fu, Z. Wei, T. Huang, A. Yu, *J. Electrochem. Soc.* **2010**, *157*, A362.

[21] M. Mirzaeian, P. J. Hall, *J. Power Sources*. **2010**, *195*, 6817.

[22] F. Mizuno, S. Nakanishi, Y. Kotani, S. Yokoishi, H. Iba, *Electrochemistry*. **2010**, *78*, 403.

[23] J. Xiao, J. Hu, D. Wang, D. Hu, W. Xu, G. L. Graff, Z. Nie, J. Liu, J. Zhang, *J. Power Sources*. **2011**, *196*, 5674.

[24] B. D. McCloskey, R. Scheffler, A. Speidel, D. S. Bethune, R. M. Shelby, A. C. Luntz, *J. Am. Chem. Soc.* **2011**, *133*, 18038.

[25] Y. Lu, D. G. Kwabi, K. P. C. Yao, J. R. Harding, J. Zhou, L. Zuin, Y. Shao-Horn, *Energy Environ. Sci.* **2011**, *4*, 2999.

[26] B. D. McCloskey, D. S. Bethune, R. M. Shelby, G. Girishkumar, A. C. Luntz, *J. Phys. Chem. Lett*. **2011**, *2*, 1161.

[27] Z. Wang, D. Xu, J. Xu, L. Zhang, X. Zhang, *Adv. Funct. Mater*. **2012**, *22*, 3699.

[28] B. M. Gallant, D. G. Kwabi, R. R. Mitchell, J. Zhou, C. V. Thompson, Y. Shao-Horn, *Energy Environ. Sci.* **2013**, *6*, 2518.

[29] C. O. Laoire, S. Mukerjee, E. J. Plichta, M. A. Hendrickson, K. M. Abraham, *J. Electrochem. Soc.* **2011**, *158*, A302.

[30] H. Jung, J. Hassoun, J. Park, Y. Sun, B. Scrosati, *Nat. Chem*. **2012**, *4*, 579.

[31] H. Jung, H. Kim, J. Park, I. Oh, J. Hassoun, C. S. Yoon, B. Scrosati, Y. Sun, *Nano Lett*. **2012**, *12*, 4333.

[32] S. H. Oh, L. F. Nazar, *Adv. Energy Mater*. **2012**, *2*, 903.

[33] S. Ma, L. Sun, L. Cong, X. Gao, C. Yao, X. Guo, L. Tai, P. Mei, Y. Zeng, H. Xie, R. Wang, *J. Phys. Chem. C*. **2013**, *117*, 25890.

[34] J. Park, J. Hassoun, H. Jung, H. Kim, C. S. Yoon, I. Oh, B. Scrosati, Y. Sun, *Nano Lett*. **2013**, *13*, 2971.

[35] G. Zhao, Z. Xu, K. Sun, *J. Mater. Chem. A*. **2013**, *1*, 12862.

[36] S. Liu, Z. Wang, C. Yu, Z. Zhao, X. Fan, Z. Ling, J. Qiu, *J. Mater. Chem. A*. **2013**, *1*, 12033.

[37] Z. Guo, D. Zhou, X. Dong, Z. Qiu, Y. Wang, Y. Xia, *Adv. Mater*. **2013**, *25*, 5668.

[38] Z. Jian, P. Liu, F. Li, P. He, X. Guo, M. Chen, H. Zhou, *Angew. Chem. Int. Ed*. **2014**, *53*, 442.

[39] Z. Zhang, G. Zhou, W. Chen, Y. Lai, J. Li, *ECS Electrochem. Lett*. **2014**, *3*, A8.

[40] C. O. Laoire, S. Mukerjee, K. M. Abraham, E. J. Plichta, M. A. Hendrickson, *J. Phys. Chem. C*. **2010**, *114*, 9178.

[41] D. Xu, Z. Wang, J. Xu, L. Zhang, X. Zhang, *Chem. Commun*. **2012**, *48*, 6948.

[42] Z. Peng, S. A. Freunberger, Y. Chen, P. G. Bruce, *Science*. **2012**, *337*, 563.

[43] S. Y. Kim, H. Lee, K. Kim, *Phys. Chem. Chem. Phys*. **2013**, *15*, 20262.

[44] M. M. Storm, M. Overgaard, R. Younesi, N. E. A. Reeler, T. Vosch, U. G. Nielsen, K. Edström, P. Norby, *Carbon*. **2015**, *85*, 233.

[45] H. Woo, J. Kang, J. Kim, C. Kim, S. Nam, B. Park, *Electron. Mater. Lett.* **2016**, *12*, 551.

[46] J. Xu, Z. Wang, D. Xu, L. Zhang, X. Zhang, *Nat Commun*. **2013**, *4*, 2438.

[47] D. Zhu, L. Zhang, M. Song, X. Wang, Y. Chen, *Chem. Commun*. **2013**, *49*, 9573.

[48] Y. Lei, J. Lu, X. Luo, T. Wu, P. Du, X. Zhang, Y. Ren, J. Wen, D. J. Miller, J. T. Miller, Y. Sun, J. W. Elam, K. Amine, *Nano Lett.* **2013**, *13*, 4182.

[49] Z. Zhang, L. Su, M. Yang, M. Hu, J. Bao, J. Wei, Z. Zhou, *Chem. Commun*. **2014**, *50*, 776.

[50] J. Park, X. Luo, J. Lu, C. D. Shin, C. S. Yoon, K. Amine, Y. Sun, *J. Phys. Chem. C*. **2015**, *119*, 15036.

[51] M. Marinaro, U. Riek, S. K. E. Moorthy, J. Bernhard, U. Kaiser, M. Wohlfahrt-Mehrens, L. Joerissen, *Electrochem. Commun*. **2013**, *37*, 53.

[52] H. Lim, H. Song, H. Gwon, K. Park, J. Kim, Y. Bae, H. Kim, S. Jung, T. Kim, Y. H. Kim, X. Lepro, R. Ovalle-Robles, R. H. Baughman, K. Kang, *Energy Environ. Sci*. **2013**, *6*, 3570.

[53] W. Chen, Z. Zhang, W. Bao, Y. Lai, J. Li, Y. Gan, J. Wang, *Electrochim. Acta*. **2014**, *134*, 293.

[54] Q. Liu, J. Xu, Z. Chang, X. Zhang, *J. Materi. Chem.Aa*. **2014**, *2*, 6081.

[55] F. Wang, Z. Wen, C. Shen, K. Rui, X. Wu, C. Chen, *J. Mater. Chem. A*. **2015**, *3*, 7600.

[56] C. Shang, S. Dong, P. Hu, J. Guan, D. Xiao, X. Chen, L. Zhang, L. Gu, G. Cui, L. Chen, *Sci. Rep.* **2015**, *5*, 8355.

[57] C. Song, B. Huang, X. Liao, X. Liu, H. Yang, Z. Ma, *J. Power Sources*. **2015**, *291*, 255.

[58] S. Wang, Y. Sha, Y. Zhu, X. Xu, Z. Shao, *J. Mater. Chem. A*. **2015**, *3*, 16132.

[59] R. Gao, L. Liu, Z. Hu, P. Zhang, X. Cao, B. Wang, X. Liu, *J. Mater. Chem. A*. **2015**, *3*, 17598.

[60] O. Oloniyo, S. Kumar, K. Scott, *J Electron Mater*. **2012**, *41*, 921.

[61] Q. Li, P. Xu, B. Zhang, H. Tsai, J. Wang, H. Wang, G. Wu, *Chem. Commun*. **2013**, *49*, 10838.

[62] R. S. Kalubarme, C. Ahn, C. Park, *Scr. Mater.* **2013**, *68*, 619.

[63] Z. H. Cui, X. X. Guo, *J. Power Sources*. **2014**, *267*, 20.

[64] L. Zhang, F. Zhang, G. Huang, J. Wang, X. Du, Y. Qin, L. Wang, *J. Power Sources*. **2014**, *261*, 311.

[65] Y. Jiang, X. Ling, Z. Jiao, L. Li, Q. Ma, M. Wu, Y. Chu, B. Zhao, *Electrochim. Acta*. **2015**, *153*, 246.

[66] S. Chen, G. Liu, H. Yadegari, H. Wang, S. Z. Qiao, *J. Mater. Chem. A*. **2015**, *3*, 2559.

[67] Y. Xu, Y. Chen, G. Xu, X. Zhang, Z. Chen, J. Li, L. Huang, K. Amine, S. Sun, *Nano Energy*. **2016**, *28*, 63.

[68] W. Luo, S. Chou, J. Wang, H. Liu, *J. Mater. Chem. A*. **2015**, *3*, 18395.

[69] W. Luo, S. Chou, J. Wang, Y. Zhai, H. Liu, *Small*. **2015**, *11*, 2817.

[70] J. Li, M. Zou, L. Chen, Z. Huang, L. Guan, *J. Mater. Chem. A*. **2014**, *2*, 10634.

[71] F. Li, R. Ohnishi, Y. Yamada, J. Kubota, K. Domen, A. Yamada, H. Zhou, *Chem. Commun.* **2013**, *49*, 1175.

[72] J. Shui, N. K. Karan, M. Balasubramanian, S. Li, D. Liu, *J. Am. Chem. Soc.* **2012**, *134*, 16654.

[73] F. Li, D. Tang, T. Zhang, K. Liao, P. He, D. Golberg, A. Yamada, H. Zhou, *Adv. Energy Mater*. **2015**, *5*, 1500294.

[74] J. Jung, K. Song, Y. Bae, S. Choi, M. Park, E. Cho, K. Kang, Y. Kang, *Nano Energy*. **2015**, *18*, 71.

[75] E. Yilmaz, C. Yogi, K. Yamanaka, T. Ohta, H. R. Byon, *Nano Letters*. **2013**, *13*, 4679.

[76] H. Jung, Y. S. Jeong, J. Park, Y. Sun, B. Scrosati, Y. J. Lee, *ACS Nano*. **2013**, *7*, 3532.

[77] P. Bhattacharya, E. N. Nasybulin, M. H. Engelhard, L. Kovarik, M. E. Bowden, X. S. Li, D. J. Gaspar, W. Xu, J. Zhang, *Adv. Funct. Mater*. **2014**, *24*, 7510.

[78] Z. Guo, D. Zhou, H. Liu, X. Dong, S. Yuan, A. Yu, Y. Wang, Y. Xia, *J. Power Sources*. **2015**, *276*, 181.

[79] P. Tan, W. Shyy, T. S. Zhao, X. B. Zhu, Z. H. Wei, *J. Mater. Chem. A*. **2015**, *3*, 19042.

[80] B. Sun, S. Chen, H. Liu, G. Wang, *Adv. Funct. Mater*. **2015**, *25*, 4436.

[81] B. Sun, L. Guo, Y. Ju, P. Munroe, E. Wang, Z. Peng, G. Wang, *Nano Energy*. **2016**, *28*, 486.

[82] Y. Chen, S. A. Freunberger, Z. Peng, O. Fontaine, P. G. Bruce, *Nat. Chem*. **2013**, *5*, 489.

[83] D. Sun, Y. Shen, W. Zhang, L. Yu, Z. Yi, W. Yin, D. Wang, Y. Huang, J. Wang, D. Wang, J. B. Goodenough, *J. Am. Chem. Soc.* **2014**, *136*, 8941.

[84] H. Lim, H. Song, J. Kim, H. Gwon, Y. Bae, K. Park, J. Hong, H. Kim, T. Kim, Y. H. Kim, X. Lepro, R. Ovalle-Robles, R. H. Baughman, K. Kang, *Angew. Chem. Int. Ed*. **2014**, *53*, 3926.

[85] B. J. Bergner, A. Schurmann, K. Peppler, A. Garsuch, J. Janek, *J. Am. Chem. Soc.* **2014**, *136*, 15054.

[86] W. Kwak, D. Hirshberg, D. Sharon, M. Afri, A. A. Frimer, H. Jung, D. Aurbach, Y. Sun, *Energy Environ. Sci*. **2016**, *9*, 2334.

[87] T. Zhang, K. Liao, P. He, H. Zhou, *Energy Environ. Sci.* **2016**, *9*, 1024.

[88] P. Gao, M. Gratzel, M. K. Nazeeruddin, *Energy Environ. Sci.* **2014**, *7*, 2448.

[89] H. Zhu, P. Zhang, S. Dai, *ACS Catal*. **2015**, *5*, 6370.

[90] H. Zhang, Y. Shimizu, Y. Teraoka, N. Miura, N. Yamazoe, *J. Catal*. **1990**, *121*, 432.

[91] H. Tanaka, M. Misono, *Curr. Opin. Solid State Mater. Sci*. **2001**, *5*, 381.

[92] T. Esaka, H. Morimoto, H. Iwahara, *J. Appl. Electrochem.* **1992**, *22*, 821.

[93] C. H. Kim, G. Qi, K. Dahlberg, W. Li, *Science*. **2010**, *327*, 1624.

[94] X. Li, W. Qu, J. Zhang, H. Wang, *J. Electrochem. Soc.* **2011**, *158*, A597.

[95] J. Zhu, H. Li, L. Zhong, P. Xiao, X. Xu, X. Yang, Z. Zhao, J. Li, *ACS Catal*. **2014**, *4*, 2917.

[96] S. J. Skinner, *Fuel Cells Bulletin*. **2001**, *4*, 6.

[97] W. Wang, C. Su, Y. Wu, R. Ran, Z. Shao, *Chem. Rev.* **2013**, *113*, 8104.

[98] A. Jun, J. Kim, J. Shin, G. Kim, *ChemElectroChem.* **2016**, *3*, 511.

[99] Z. Gao, L. V. Mogni, E. C. Miller, J. G. Railsback, S. A. Barnett, *Energy Environ. Sci*. **2016**, *9*, 1602.

[100] D. Chen, C. Chen, Z. M. Baiyee, Z. Shao, F. Ciucci, *Chem. Rev.* **2015**, *115*, 9869.

[101] F. Bidault, D. J. L. Brett, P. H. Middleton, N. P. Brandon, *J. Power Sources*. **2009**, *187*, 39.

[102] V. Neburchilov, H. Wang, J. J. Martin, W. Qu, *J. Power Sources*. **2010**, *195*, 1271.

[103] M. Song, S. Park, F. M. Alamgir, J. Cho, M. Liu, *Mater. Sci. Eng. R-Rep.* **2011**, *72*, 203.

[104] L. J. Hardwick, P. G. Bruce, *Curr. Opin. Solid State Mater. Sci*. **2012**, *16*, 178.

[105] Q. Li, R. Cao, J. Cho, G. Wu, *Phys. Chem. Chem. Phys*. **2014**, *16*, 13568.

[106] N. Mahmood, C. Zhang, H. Yin, Y. Hou, *J. Mater. Chem. A.* **2014**, *2*, 15.

[107] Z. Wen, C. Shen, Y. Lu, *ChemPlusChem*. **2015**, *80*, 270.

[108] Z. Ma, X. Yuan, L. Li, Z. Ma, D. P. Wilkinson, L. Zhang, J. Zhang, *Energy Environ. Sci*. **2015**, *8*, 2144.

[109] Z. Chang, J. Xu, Q. Liu, L. Li, X. Zhang, *Adv. Energy Mater.* **2015**, *5*, 1500633.

[110] C. O. Laoire, S. Mukerjee, K. M. Abraham, E. J. Plichta, M. A. Hendrickson, *J. Phys. Chem. C*. **2009**, *113*, 20127.

[111] N. Ding, S. W. Chien, T. S. A. Hor, R. Lum, Y. Zong, Z. Liu, *J. Mater. Chem. A.* **2014**, *2*, 12433.

[112] C. Yang, R. A. Wong, M. Hong, K. Yamanaka, T. Ohta, H. R. Byon, *Nano Lett.* **2016**, *16*, 2969.

[113] C. N. Chervin, M. J. Wattendorf, J. W. Long, N. W. Kucko, D. R. Rolison, *J. Electrochem. Soc.* **2013**, *160*, A1510.

[114] P. Tan, W. Shyy, L. An, Z. H. Wei, T. S. Zhao, *Electrochem. Commun*. **2014**, *46*, 111.

[115] R. R. Mitchell, B. M. Gallant, Y. Shao-Horn, C. V. Thompson, *J. Phys. Chem. Lett*. **2013**, *4*, 1060.

[116] Y. Cui, Z. Wen, Y. Liu, *Energy Environ. Sci*. **2011**, *4*, 4727.

[117] M. M. O. Thotiyl, S. A. Freunberger, Z. Peng, Y. Chen, Z. Liu, P. G. Bruce, *Nat. Mater*. **2013**, *12*, 1049.

[118] J. Xu, Z. Chang, Y. Wang, D. Liu, Y. Zhang, X. Zhang, *Adv Mater*. **2016**, *28*, 9620

[119] A. Khetan, A. Luntz, V. Viswanathan, *J. Phys. Chem. Lett.* **2015**, *6*, 1254.

[120] L. Johnson, C. Li, Z. Liu, Y. Chen, S. A. Freunberger, P. C. Ashok, B. B. Praveen, K. Dholakia, J. Tarascon, P. G. Bruce, *Nat Chem*. **2014**, *6*, 1091.

[121] D. Aurbach, B. D. McCloskey, L. F. Nazar, P. G. Bruce, *Nat. Energy*. **2016**, *1*, 16128.

[122] A. Luntz, V. Viswanathan, J. Voss, J. Varley, J. Nørskov, R. Scheffler, A. Speidel, *J. Phys. Chem. Lett*. **2013**, *4*, 3494.

[123] M. del Pozo, W. R. Torres, S. E. Herrera, E. J. Calvo, *ChemElectroChem*. **2016**, *3*, 1.

[124] C. M. Burke, V. Pande, A. Khetan, V. Viswanathan, B. D. McCloskey, *Proc. Natl. Acad. Sci.* **2015**, *112*, 9293.

[125] K. M. Abraham, *J. Electrochem. Soc*. **2015**, *162*, A3021.

[126] N. B. Aetukuri, B. D. McCloskey, J. M. Garcia, L. E. Krupp, V. Viswanathan, A. C. Luntz, *Nat Chem*. **2015**, *7*, 50.

[127] D. Sharon, D. Hirsberg, M. Salama, M. Afri, A. A. Frimer, M. Noked, W. Kwak, Y. Sun, D. Aurbach, *ACS Appl. Mater. Interfaces*. **2016**, *8*, 5300.

[128] J. Lu, Y. J. Lee, X. Luo, K. C. Lau, M. Asadi, H. Wang, S. Brombosz, J. Wen, D. Zhai, Z. Chen, D. J. Miller, Y. S. Jeong, J. Park, Z. Z. Fang, B. Kumar, A. Salehi-Khojin, Y. Sun, L. A. Curtiss, K. Amine, *Nature*. **2016**, *529*, 377.

[129] Y. Yang, T. Zhang, X. Wang, L. Chen, N. Wu, W. Liu, H. Lu, L. Xiao, L. Fu, L. Zhuang, *ACS Appl. Mater. Interfaces*. **2016**, *8*, 21350.

[130] Z. Liu, L. R. De Jesus, S. Banerjee, P. P. Mukherjee, *ACS Appl. Mater. Interfaces* **2016**, *8*, 23028.

[131] W. Fan, B. Wang, X. Guo, X. Kong, J. Liu, *Nano Energy*. **2016**, *27*, 577.

[132] Y. Zhao, L. Xu, L. Mai, C. Han, Q. An, X. Xu, X. Liu, Q. Zhang, *Proc. Natl. Acad. Sci.* **2012**, *109*, 19569.

[133] J. Cheng, M. Zhang, Y. Jiang, L. Zou, Y. Gong, B. Chi, J. Pu, L. Jian, *Electrochim. Acta*. **2016**, *191*, 106.

[134] J. Suntivich, H. A. Gasteiger, N. Yabuuchi, H. Nakanishi, J. B. Goodenough, Y. Shao-Horn, *Nat. Chem*. **2011**, *3*, 546.

[135] X. Ge, F. T. Goh, B. Li, T. A. Hor, J. Zhang, P. Xiao, X. Wang, Y. Zong, Z. Liu, *Nanoscale*. **2015**, *7*, 9046.

[136] H. Yin, C. Zhang, F. Liu, Y. Hou, *Adv. Funct. Mater*. **2014**, *24*, 2930.

[137] J. Kim, X. Yin, K. Tsao, S. Fang, H. Yang, *J. Am. Chem. Soc.* **2014**, *136*, 14646.

[138] Y. Lee, J. Kleis, J. Rossmeisl, Y. Shao-Horn, D. Morgan, *Energy Environ. Sci*. **2011**, *4*, 3966.

[139] P. Tan, W. Shyy, T. S. Zhao, Z. H. Wei, L. An, *J. Power Sources*. **2015**, *278*, 133.

[140] J. Xie, Q. Dong, I. Madden, X. Yao, Q. Cheng, P. Dornath, W. Fan, D. Wang, *Nano Lett*. **2015**, *15*, 8371.

[141] V. Viswanathan, K. S. Thygesen, J. S. Hummelshoj, J. K. Norskov, G. Girishkumar, B. D. McCloskey, A. C. Luntz, *J. Chem. Phys.* **2011**, *135*, 214704.

[142] B. D. McCloskey, C. M. Burke, J. E. Nichols, S. E. Renfrew, *Chem. Commun*. **2015**, *51*, 12701.

[143] N. Feng, P. He, H. Zhou, *Adv. Energy Mater.* **2016**, *6*, 1502303.

[144] J. R. Harding, Y. Lu, Y. Tsukada, Y. Shao-Horn, *Phys. Chem. Chem. Phys.* **2012**, *14*, 10540.

[145] Y. Lu, Y. Shao-Horn, *J. Phys. Chem. Lett*. **2013**, *4*, 93.

[146] J. S. Hummelshoj, A. C. Luntz, J. K. Norskov, *J. Chem. Phys.* **2013**, *138*, 034703.

[147] S. Ganapathy, B. D. Adams, G. Stenou, M. S. Anastasaki, K. Goubitz, X. Miao, L. F. Nazar, M. Wagemaker, *J. Am. Chem. Soc.* **2014**, *136*, 16335.

[148] D. Zhai, H. Wang, J. Yang, K. C. Lau, K. Li, K. Amine, L. A. Curtiss, *J. Am. Chem. Soc*. **2013**, *135*, 15364.

[149] D. Zhai, H. Wang, K. C. Lau, J. Gao, P. C. Redfern, F. Kang, B. Li, E. Indacochea, U. Das, H. Sun, H. Sun, K. Amine, L. A. Curtiss, *J. Phys. Chem. Lett.* **2014**, *5*, 2705.

[150] D. Zhai, K. C. Lau, H. Wang, J. Wen, D. J. Miller, J. Lu, F. Kang, B. Li, W. Yang, J. Gao, E. Indacochea, L. A. Curtiss, K. Amine, *Nano Lett*. **2015**, *15*, 1041.

[151] C. Xia, M. Waletzko, L. Chen, K. Peppler, P. J. Klar, J. Janek, *ACS Appl. Mater. Interfaces*. **2014**, *6*, 12083.

[152] Y. Hu, X. Han, F. Cheng, Q. Zhao, Z. Hu, J. Chen, *Nanoscale*. **2014**, *6*, 177.

[153] R. Black, J. Lee, B. Adams, C. A. Mims, L. F. Nazar, *Angew. Chem. Int. Ed.* **2013**, *52*, 392.

[154] J. Suntivich, K. J. May, H. A. Gasteiger, J. B. Goodenough, Y. Shao-Horn, *Science*. **2011**, *334*, 1383.

[155] Z. Shao, S. M. Haile, *Nature*. **2004**, *431*, 170.

[156] J. Jung, H. Y. Jeong, J. Lee, M. G. Kim, J. Cho, *Angew. Chem. Int. Ed.* **2014**, *53*, 4582.

[157] K. P. C. Yao, Y. Lu, C. V. Amanchukwu, D. G. Kwabi, M. Risch, J. Zhou, A. Grimaud, P. T. Hammond, F. Barde, Y. Shao-Horn, *Phys. Chem. Chem. Phys*. **2014**, *16*, 2297.

[158] Y. Lu, Z. Xu, H. A. Gasteiger, S. Chen, K. Hamad-Schifferli, Y. Shao-Horn, *J. Am. Chem. Soc.* **2010**, *132*, 12170.

[159] Y. Lu, H. A. Gasteiger, E. Crumlin, R. McGuire Jr., Y. Shao-Horn, *J. Electrochem. Soc.* **2010**, *157*, A1016.

[160] H. Cheng, K. Scott, *Appl. Catal. B: Environ*. **2011**, *108*, 140.

[161] Y. Yang, M. Shi, Q. Zhou, Y. Li, Z. Fu, *Electrochem. Commun*. **2012**, *20*, 11.

[162] J. Yin, B. Fang, J. Luo, B. Wanjala, D. Mott, R. Loukrakpam, M. S. Ng, Z. Li, J. Hong, M. S. Whittingham, C. Zhong, *Nanotechnology*. **2012**, *23*, 495602.

[163] A. K. Thapa, T. H. Shin, S. Ida, G. U. Sumanasekera, M. K. Sunkara, T. Ishihara, *J. Power Sources*. **2012**, *220*, 211.

[164] K. P. C. Yao, M. Risch, S. Y. Sayed, Y. Lee, J. R. Harding, A. Grimaud, N. Pour, Z. Xu, J. Zhou, A. Mansour, F. Barde, Y. Shao-Horn, *Energy Environ. Sci.* **2015**, *8*, 2417.

[165] Y. Gan, Y. Lai, Z. Zhang, W. Chen, K. Du, J. Li, *J. Alloys Compounds*. **2016**, *665*, 365.

[166] X. Zhang, D. Han, Y. He, D. Zhai, D. Liu, H. Du, B. Li, F. Kang, *J. Mater. Chem. A*. **2016**, *4*, 7727.

[167] Y. Zheng, K. Song, J. Jung, C. Li, Y. Heo, M. Park, M. Cho, Y. Kang, K. Cho, *Chem. Mater*. **2015**, *27*, 3243.

[168] J. Zhu, X. Ren, J. Liu, W. Zhang, Z. Wen, *ACS Catal*. **2015**, *5*, 73.

[169] J. Zhu, F. Wang, B. Wang, Y. Wang, J. Liu, W. Zhang, Z. Wen, *J. Am. Chem. Soc.* **2015**, *137*, 13572.

[170] H. Kwon, J. W. Han, *J. Korean Chem. Soc*. **2016**, *53*, 306.

[171] Q. Xu, X. Han, F. Ding, L. Zhang, L. Sang, X. Liu, Q. Xu, *J. Alloys Compounds*. **2016**, *664*, 750.

[172] Q. Xu, S. Song, Y. Zhang, Y. Wang, J. Zhang, Y. Ruan, M. Han, *Electrochim. Acta*. **2016**, *191*, 577.

[173] Z. Fu, X. Lin, T. Huang, A. Yu, *J. Solid State Electr*. **2012**, *16*, 1447.

[174] Q. Song, C. Chiu, S. Chan, *J. Appl. Electrochem.* **2006**, *36*, 97.

[175] J. J. Lee, M. Y. Oh, K. S. Nahm, *J. Electrochem. Soc.* **2016**, *163*, A244.

[176] N. Tian, Z. Y. Zhou, S. G. Sun, Y. Ding, Z. L. Wang, *Science*. **2007**, *316*, 732.

[177] H. Wang, H. Lee, Y. Deng, Z. Lu, P. Hsu, Y. Liu, D. Lin, Y. Cui, *Nat. Commun*. **2015**, *6*, 7261.

[178] J. Lee, R. Black, G. Popov, E. Pomerantseva, F. Nan, G. A. Botton, L. F. Nazar, *Energy Environ. Sci*. **2012**, *5*, 9558.

[179] C. Francia, J. Amici, E. Tasarkuyu, A. Çoşkun, Ö F. Gül, T. Şener, *Int J Hydrogen Energy*. **2016**, *41*, 20583.

[180] Z. Du, P. Yang, L. Wang, Y. Lu, J. B. Goodenough, J. Zhang, D. Zhang, *J. Power Sources*. **2014**, *265*, 91.

[181] N. Sun, H. Liu, Z. Yu, Z. Zheng, C. Shao, *RSC Adv*. **2016**, *6*, 13522.

[182] N. Sun, H. Liu, Z. Yu, Z. Zheng, C. Shao, *Ionics*. **2016**, *22*, 869.

[183] Z. Wang, Y. You, J. Yuan, Y. Yin, Y. Li, S. Xin, D. Zhang, *ACS Appl. Mater. Interfaces*. **2016**, *8*, 6520.

[184] R. S. Kalubarme, G. Park, K. Jung, K. Shin, W. Ryu, C. Park, *J. Electrochem. Soc.* **2014**, *161*, A880.

[185] K. Jung, J. Lee, W. B. Im, S. Yoon, K. Shin, J. Lee, *Chem. Commun*. **2012**, *48*, 9406.

[186] Z. Ma, X. Yuan, L. Li, Z. Ma, *Chem. Commun.* **2014**, *50*, 14855.

[187] P. Tan, W. Shyy, Z. H. Wei, L. An, T. S. Zhao, *Electrochim. Acta*. **2014**, *147*, 1.

[188] Q. Li, N. Mahmood, J. Zhu, Y. Hou, S. Sun, *Nano Today*. **2014**, *9*, 668.

[189] S. H. Oh, R. Black, E. Pomerantseva, J. Lee, L. F. Nazar, *Nat. Chem*. **2012**, *4*, 1004.

[190] T. Y. Ma, Y. Zheng, S. Dai, M. Jaroniec, S. Z. Qiao, *J. Mater. Chem. A*. **2014**, *2*, 8676.

[191] F. Cheng, J. Chen, *Nat. Chem*. **2012**, *4*, 962.

[192] N. Sun, H. Liu, Z. Yu, Z. Zheng, C. Shao, *Solid State Ionics*. **2014**, *268*, 125.

[193] C. Jin, Z. Yang, X. Cao, F. Lu, R. Yang, *Int J Hydrogen Energy*. **2014**, *39*, 2530.

[194] X. Han, Y. Hu, J. Yang, F. Cheng, J. Chen, *Chem. Commun*. **2014**, *50*, 1497.

[195] J. Xu, Z. Wang, D. Xu, F. Meng, X. Zhang, *Energy Environ. Sci.* **2014**, *7*, 2213.

[196] M. Y. Oh, J. J. Lee, A. Zahoor, K. S. Nahm, *RSC Adv*. **2016**, *6*, 32212.

[197] J. Xu, D. Xu, Z. Wang, H. Wang, L. Zhang, X. Zhang, *Angew. Chem. Int. Ed.* **2013**, *52*, 3887.

[198] G. Liu, H. Chen, L. Xia, S. Wang, L. Ding, D. Li, K. Xiao, S. Dai, H. Wang, *ACS Appl. Mater. Interfaces.* **2015**, *7*, 22478.

[199] P. Li, J. Zhang, Q. Yu, J. Qiao, Z. Wang, D. Rooney, W. Sun, K. Sun, *Electrochim. Acta*. **2015**, *165*, 78.

[200] F. Lu, Y. Wang, C. Jin, F. Li, R. Yang, F. Chen, *J. Power Sources*. **2015**, *293*, 726.

[201] J. Zhang, Y. Zhao, X. Zhao, Z. Liu, W. Chen, *Sci. Rep.* **2014**, *4*, 6005.

[202] T. Zhang, H. Zhou, *Nat. Commun*. **2013**, *4*, 1817.

[203] A. Débart, A. J. Paterson, J. Bao, P. G. Bruce, *Angew. Chem*. **2008**, *120*, 4597.

[204] K. Liao, X. Wang, Y. Sun, D. Tang, M. Han, P. He, X. Jiang, T. Zhang, H. Zhou, *Energy Environ. Sci.* **2015**, *8*, 1992.

[205] J. Lu, L. Li, J. Park, Y. Sun, F. Wu, K. Amine, *Chem. Rev.* **2014**, *114*, 5611.

[206] B. D. McCloskey, A. Speidel, R. Scheffler, D. C. Miller, V. Viswanathan, J. S. Hummelshoj, J. K. Norskov, A. C. Luntz, *J. Phys. Chem. Lett*. **2012**, *3*, 997.

[207] M. M. Ottakam Thotiyl, S. A. Freunberger, Z. Peng, P. G. Bruce, *J. Am. Chem. Soc.* **2013**, *135*, 494.

[208] R. Black, S. H. Oh, J. Lee, T. Yim, B. Adams, L. F. Nazar, *J. Am. Chem. Soc.* **2012**, *134*, 2902.

[209] Z. Wei, T. Zhao, X. Zhu, L. An, P. Tan, *Energy Technology*. **2015**, *3*, 1093.

[210] J. Lu, Y. Lei, K. C. Lau, X. Luo, P. Du, J. Wen, R. S. Assary, U. Das, D. J. Miller, J. W. Elam, H. M. Albishri, D. Abd El-Hady, Y. Sun, L. A. Curtiss, K. Amine, *Nat Commun*. **2013**, *4*, 2383.

[211] Y. Cao, M. Zheng, S. Cai, X. Lin, C. Yang, W. Hu, Q. Dong, *J. Mater. Chem. A*. **2014**, *2*, 18736.

[212] S. J. Kang, T. Mori, S. Narizuka, W. Wilcke, H. Kim, *Nat. Commun*. **2014**, *5*, 3937.

[213] L. Nazar, D. Kundu, R. Black, E. Jamstorp, *Energy Environ. Sci.* **2014**, *8*, 1292.

[214] B. Liu, P. Yan, W. Xu, J. Zheng, Y. He, L. Luo, M. E. Bowden, C. Wang, J. Zhang, *Nano Lett*. **2016**, *16*, 4932.

[215] M. Yuasa, T. Matsuyoshi, T. Kida, K. Shimanoe, *J. Power Sources*. **2013**, *242*, 216.

[216] Y. Shao, F. Ding, J. Xiao, J. Zhang, W. Xu, S. Park, J. Zhang, Y. Wang, J. Liu, *Adv. Funct. Mater*. **2013**, *23*, 987.

[217] T. Meng, M. Ara, L. Wang, R. Naik, K. S. Ng, *J. Mater. Sci.* **2014**, *49*, 4058.

[218] S. Khan, R. J. Oldman, C. R. A. Catlow, S. A. French, S. A. Axon, *J. Phys. Chem. C*. **2008**, *112*, 12310.

[219] Q. Wei, R. Guo, F. Wang, H. Li, *J. Mater. Sci.* **2005**, *40*, 1317.

[220] M. Lu, C. Xu, Y. Zhan, J. Y. Lee, *Chemistry–An Asian Journal*. **2016**, *11*, 1210.

[221] Y. Yang, W. Yin, S. Wu, X. Yang, W. Xia, Y. Shen, Y. Huang, A. Cao, Q. Yuan, *ACS Nano*. **2015**, *10*, 1240.

[222] K. R. Yoon, D. S. Kim, W. Ryu, S. H. Song, D. Youn, J. Jung, S. Jeon, Y. J. Park, I. Kim, *ChemSusChem*. **2016**, *9*, 2080.

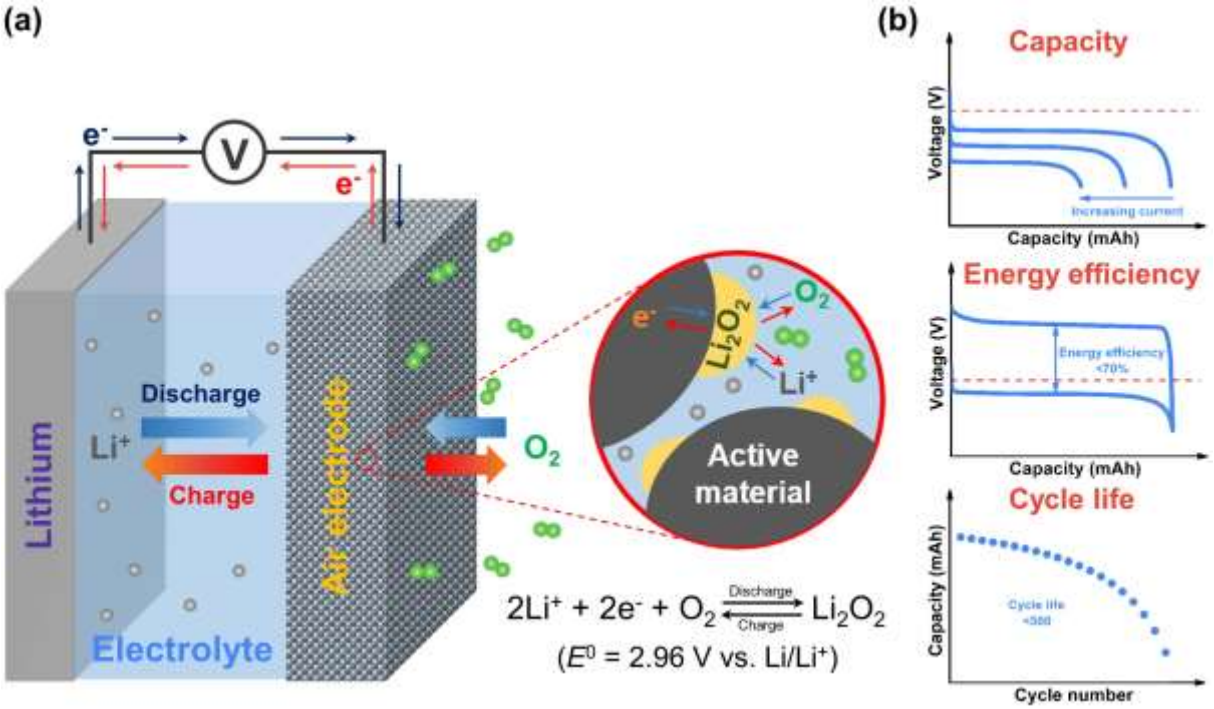

Figure 1. a) A schematic representation of a non-aqueous lithium-air battery. b) Main challenges in the battery performance.

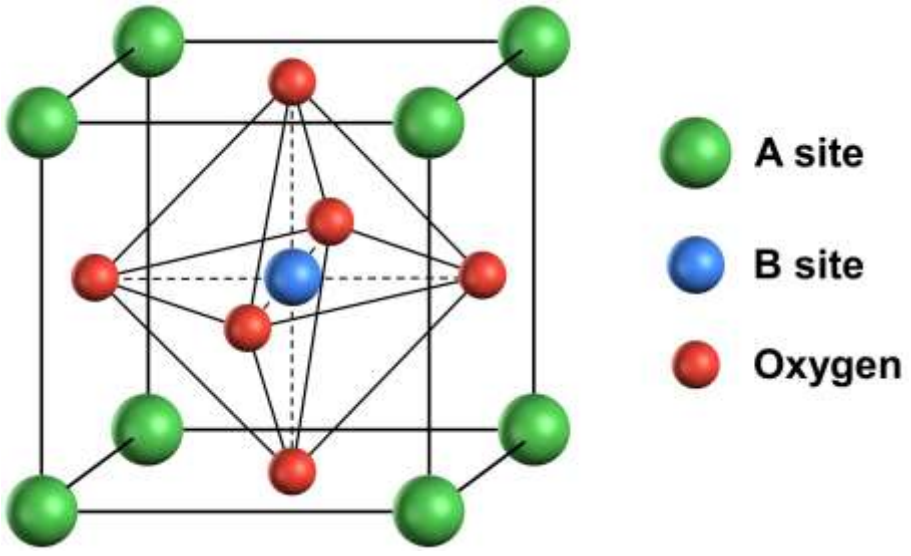

Figure 2. Schematic illustration of an ideal unit cell of perovskite oxide, where A is a rare-earth or alkaline-earth metal and B is a transition-metal.

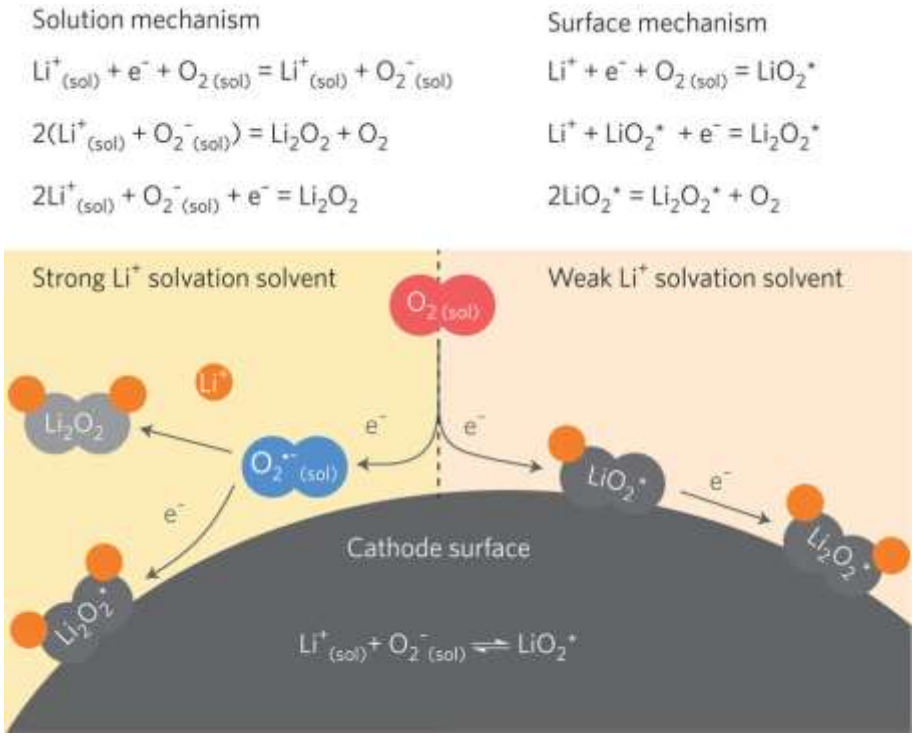

Figure 3. Oxygen reduction mechanisms in a non-aqueous lithium-oxygen battery at low overpotentials. Reproduced with permission.[121] Copyright 2016, Macmillan Publishers Limited.

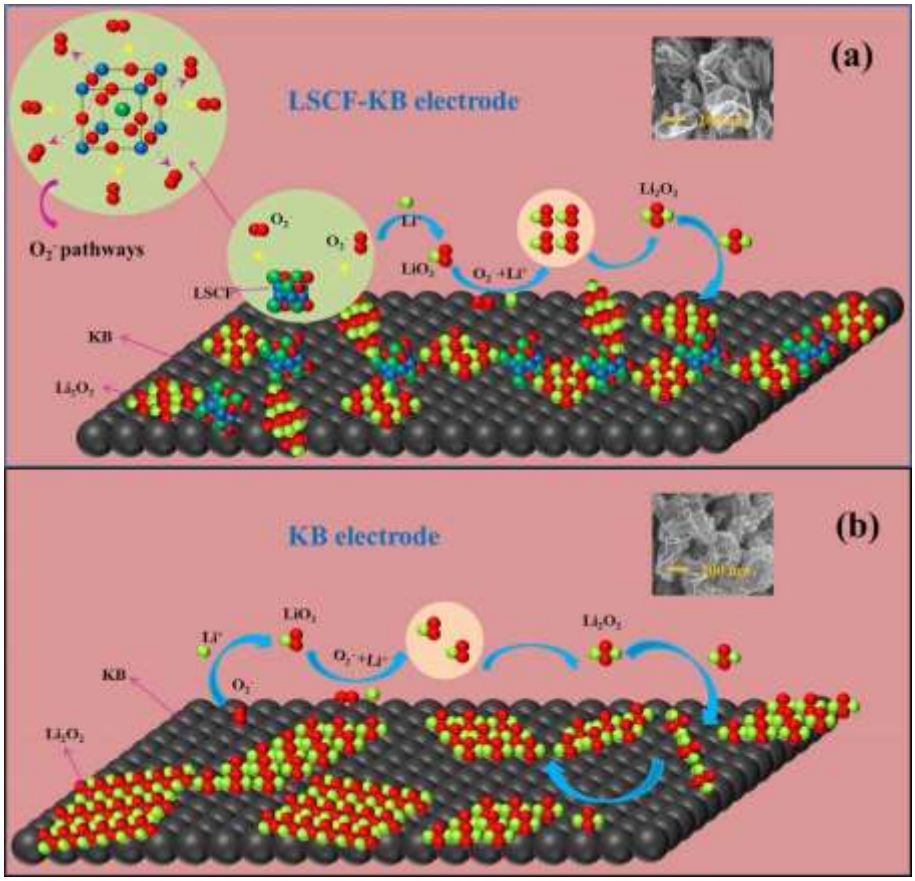

Figure 4. Illustration of the formation processes of Li_2O_2 at a) LSCF-KB and b) KB electrode. Reproduced with permission.[133] Copyright 2016, Elsevier, B.V.

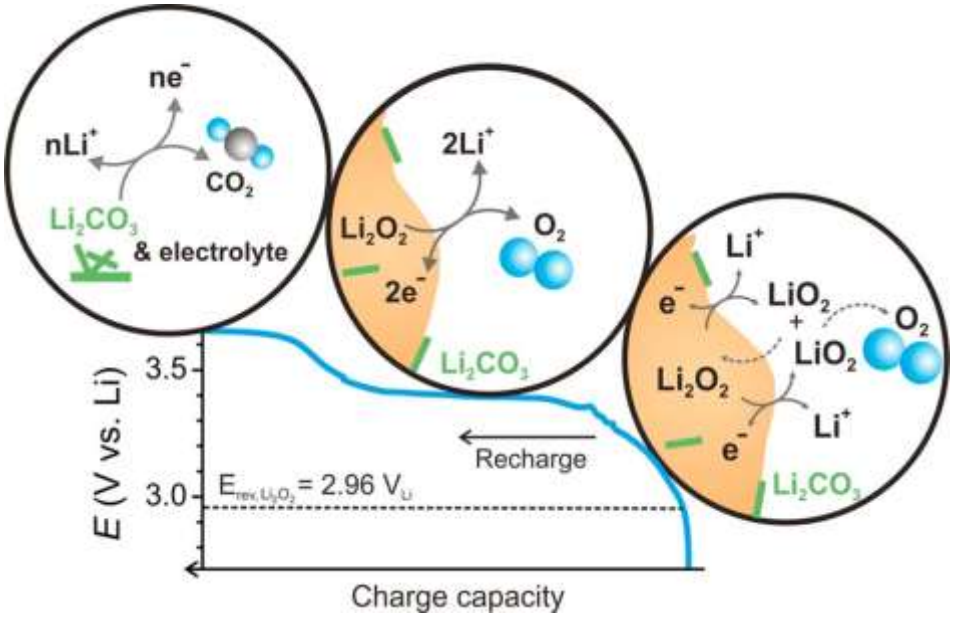

Figure 5. A proposed charge mechanism in a non-aqueous lithium-oxygen battery. Reproduced with permission.[145] Copyright 2013, American Chemical Society.

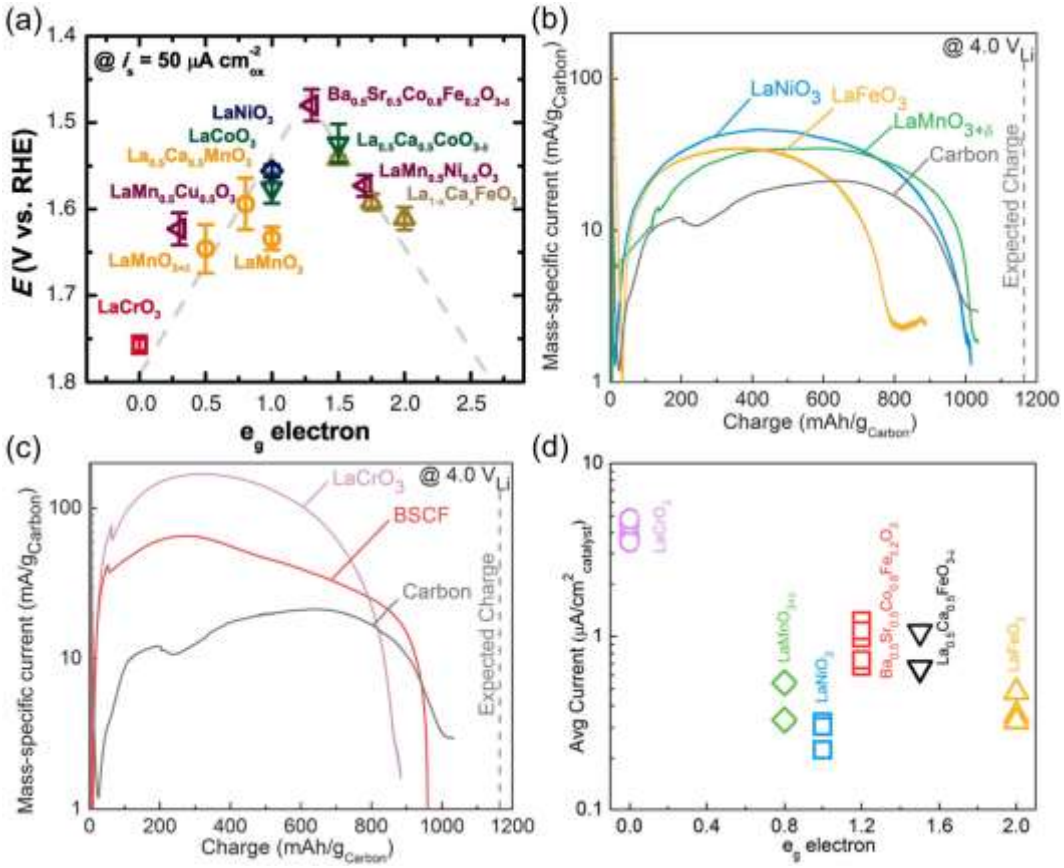

Figure 6. a) OER catalytic activity of various perovskite oxides versus e_g-filling in 0.1 M KOH. Reproduced with permission.[154] Copyright 2011, American Association for the Advancement of Science. b-d) Net current of Li_2O_2 oxidation normalized to carbon mass of Li_2O_2-preloaded electrodes with b) $LaFeO_3$, $LaNiO_3$, $LaMnO_{3+\delta}$, and c) $LaCrO_3$ and BSCF compared to VC electrodes. d) catalyst-area specific activity of various perovskite oxides in oxidizing Li_2O_2 versus reported oxide e_g-filling. Reproduced with permission.[157] Copyright 2014, The Royal Society of Chemistry.

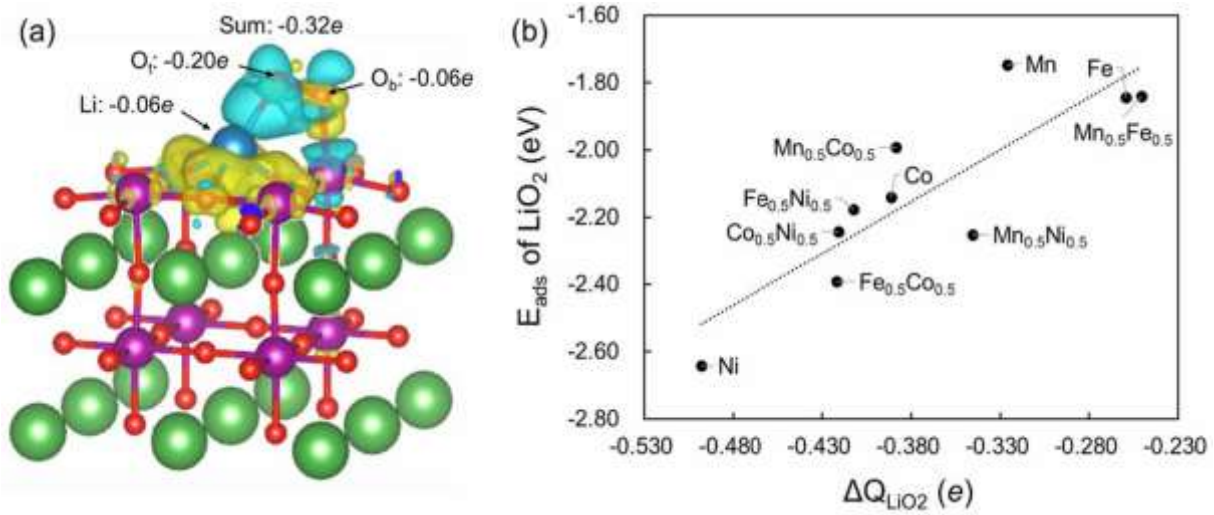

Figure 7. a) Changes in the electron density upon LiO_2 adsorption on $LaMnO_3$(001). Yellow and cyan colors indicate decreased and increased electron densities, respectively. O_t and O_b indicate the atomic oxygens located at the top and bottom of the adsorbed LiO_2 molecule, respectively. b) Adsorption energies as a function of the charge density differences on the LiO_2 adsorbed $LaB_{1-x}B'_xO_3$(001) (B, B' = Mn, Fe, Co, and Ni, x = 0.0, 0.5). Reproduced with permission.[170] Copyright 2016, Korean Ceramic Society.

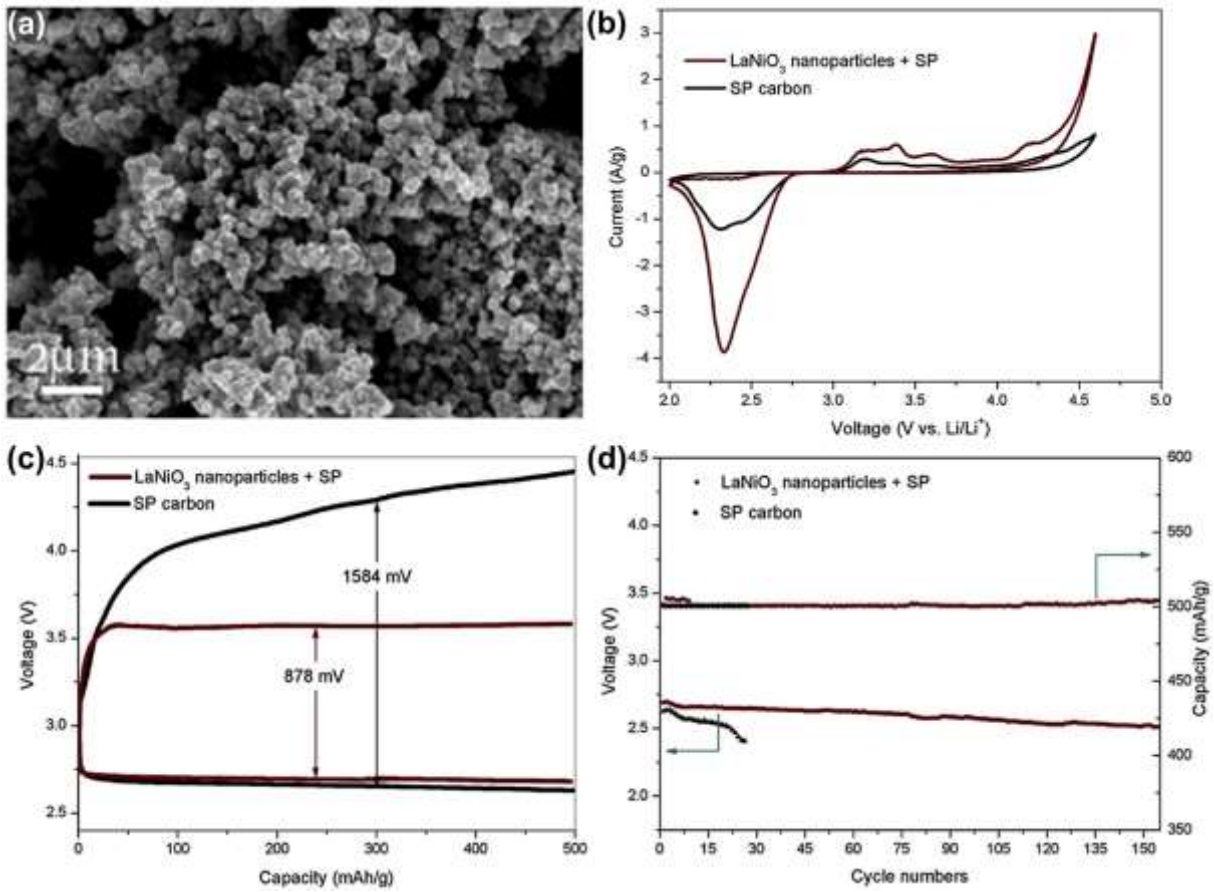

Figure 8. a) SEM images of $LaNiO_3$ nanoparticles. b) CV curves of $LaNiO_3$/SP and SP electrode at a scan rate of 0.1 mV s^{-1} in a 1.0 M LITFSI/TEGDME electrolyte. c-d) Performance of lithium-oxygen batteries with $LaNiO_3$/SP or SP electrodes: c) discharge-charge voltage profiles at a current density of 50 mA g^{-1} and d) discharge voltage versus cycle number at 100 mA g^{-1}. Reproduced with permission.[171] Copyright 2016, Elsevier, B.V.

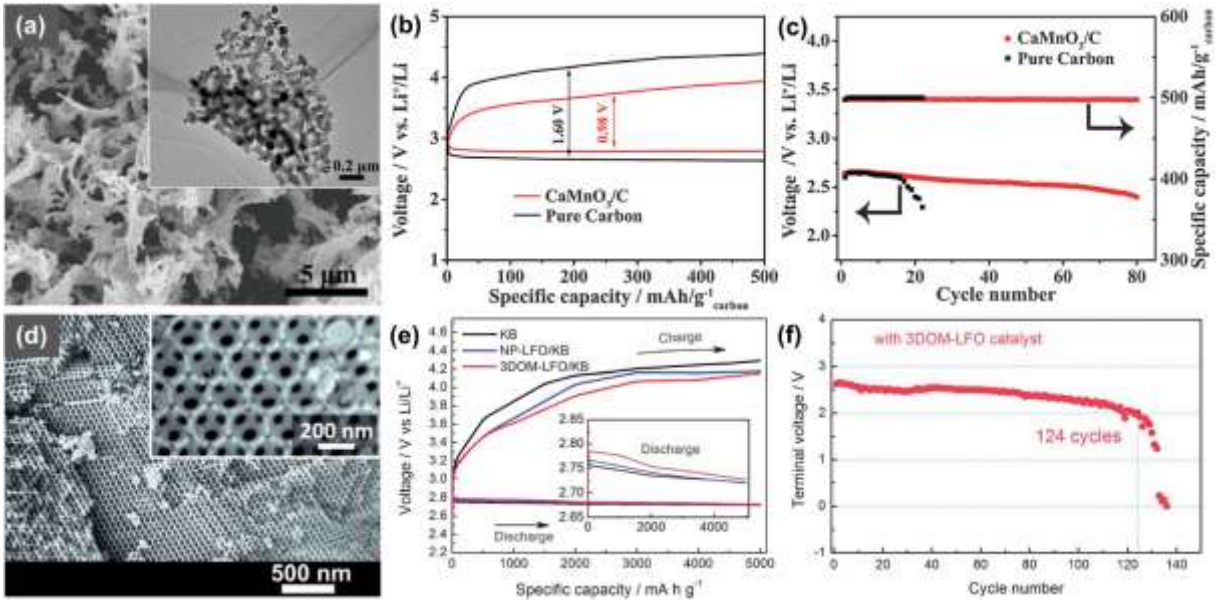

Figure 9. Characterization of macroporous perovskite oxide made of a-c) $CaMnO_3$. Reproduced with permission.[194] Copyright 2014, The Royal Society of Chemistry. d-f) $LaFeO_3$. Reproduced with permission.[195] Copyright 2014, The Royal Society of Chemistry. a and d) SEM image, inset shows the transmission electron microscopy (TEM) image. b and e) Discharge and charge profiles of non-aqueous lithium-oxygen batteries with different oxygen electrodes. c and f) Discharge voltage versus cycle number. All batteries were with 1.0 M LITFSI/TEGDME electrolytes and tested in pure oxygen atmosphere.

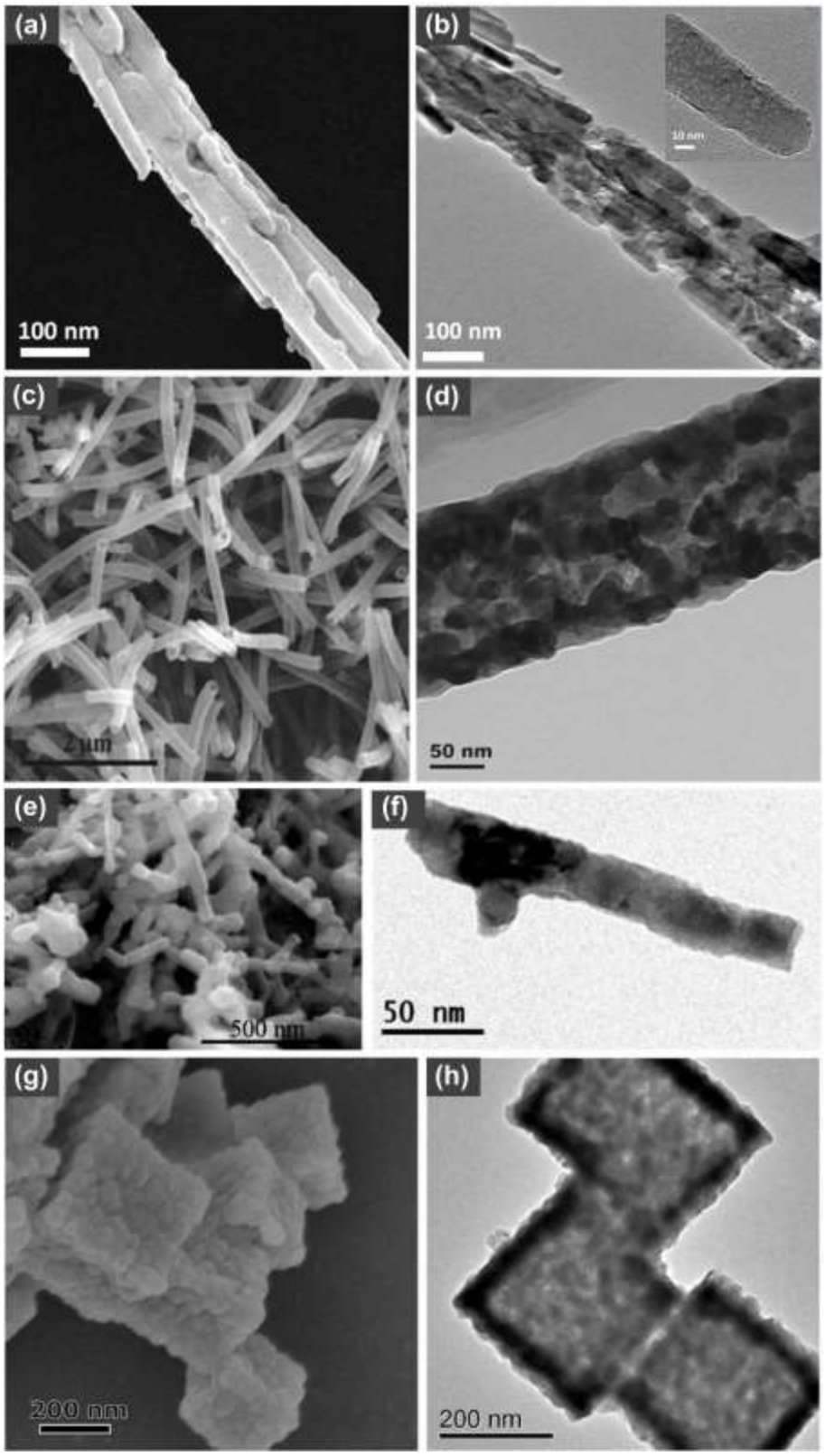

Figure 10. SEM and TEM images of: a-b) hierarchical mesoporous $La_{0.5}Sr_{0.5}CoO_{2.91}$ nanowires. Reproduced with permission.[132] Copyright 2012, National Academy of Sciences. c-d) $La_{0.5}Sr_{0.5}CoO_{2.91}$ nanotubes. Reproduced with permission.[199] Copyright 2015, Elsevier, B.V. e-f) $La_{0.8}Sr_{0.2}MnO_3$ nanorods. Reproduced with permission.[200] Copyright 2015, Elsevier, B.V. g-h) $LaNiO_3$ nanotubes. Reproduced with permission.[201] Copyright 2014, Macmillan Publishers Limited.

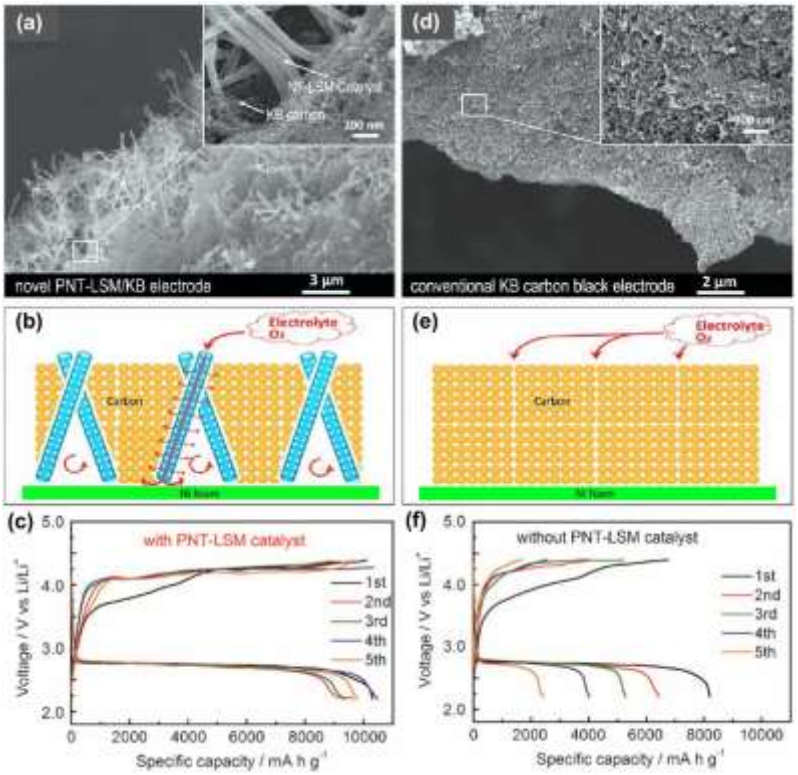

Figure 11. Characterization of the oxygen electrode made of a-c) NT-LSM/KB and d-f) KB: a and d) SEM images. b and e) Schematic illustration of the structures. c and f) Cyclic performance at a current density of 0.025 mA cm^{-2} within a voltage range of 2.2−4.4 V. Reproduced with permission.[197] Copyright 2013, Wiley-VCH Verlag GmbH & Co. KGaA, Weinheim.

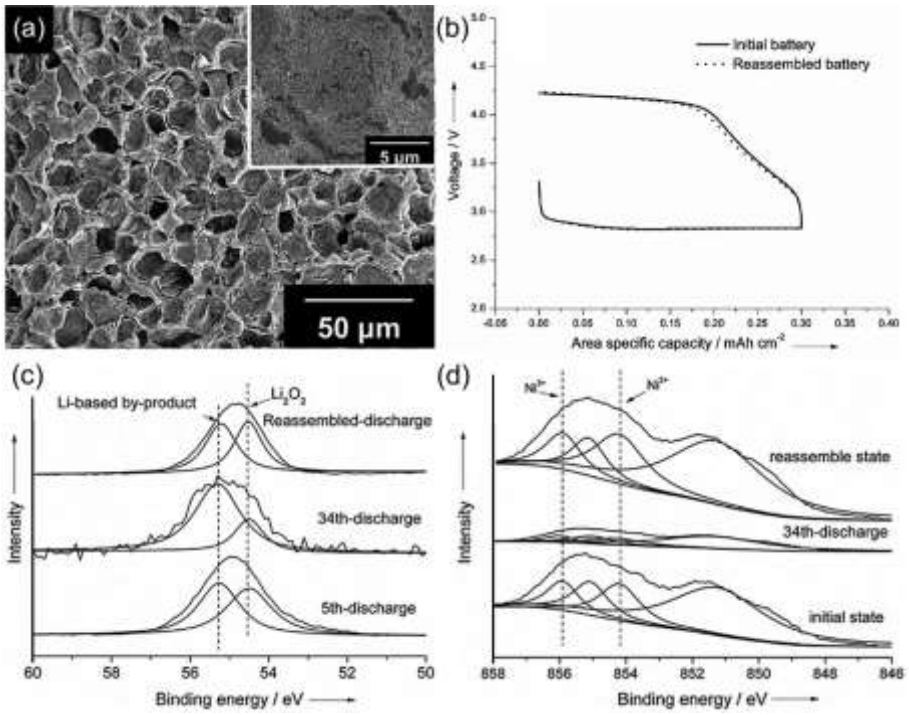

Figure 12. a) SEM image of the integrated electrode made of $LaNiO_3$, the inset shows the microstructure of the nested pores. b) Voltage profiles of the initial and reassembled batteries with the integrated electrode. c) Li 1s XPS spectra of discharge products at different states; and d) Ni 2p XPS spectra of the $LaNiO_3$ electrode at different states. Reproduced with permission.[209] Copyright 2015, Wiley-VCH Verlag GmbH & Co. KGaA, Weinheim.

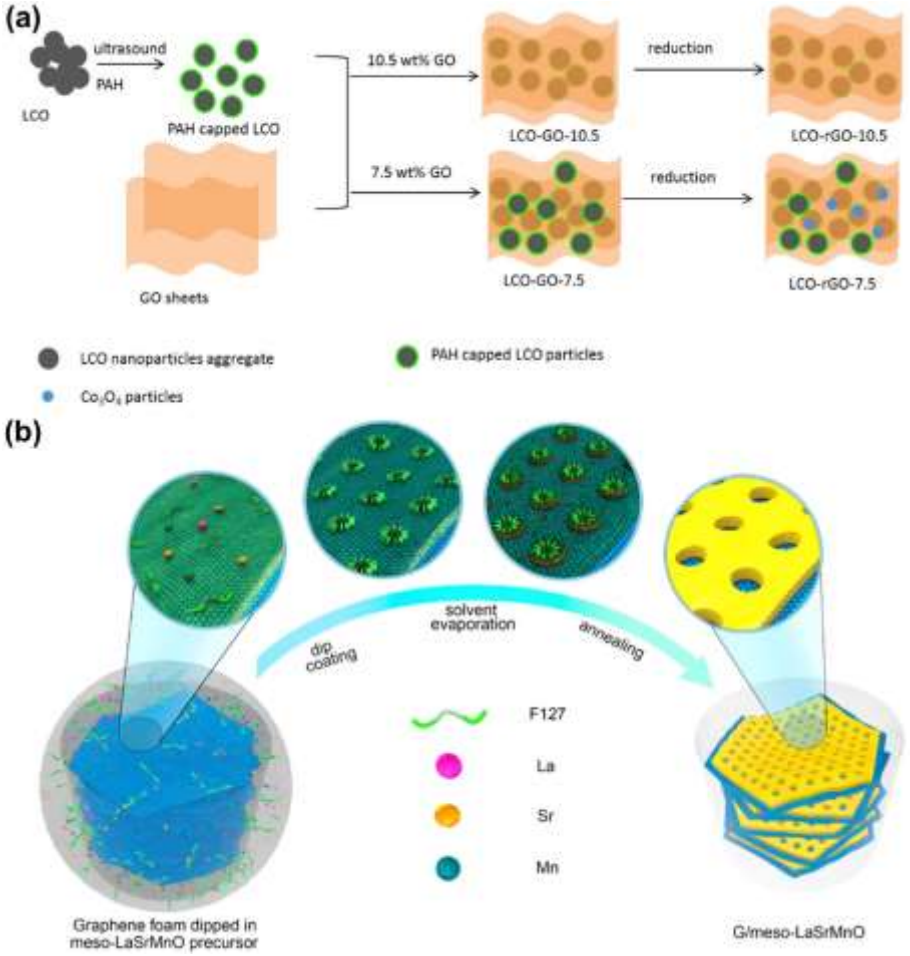

Figure 13. Illustration of the fabrication process of a) LCO-rGO composites. Reproduced with permission.[220] Copyright 2016, Wiley-VCH Verlag GmbH & Co. KGaA, Weinheim. b) G/meso-LaSrMnO Foams. Reproduced with permission.[221] Copyright 2015, American Chemical Society.

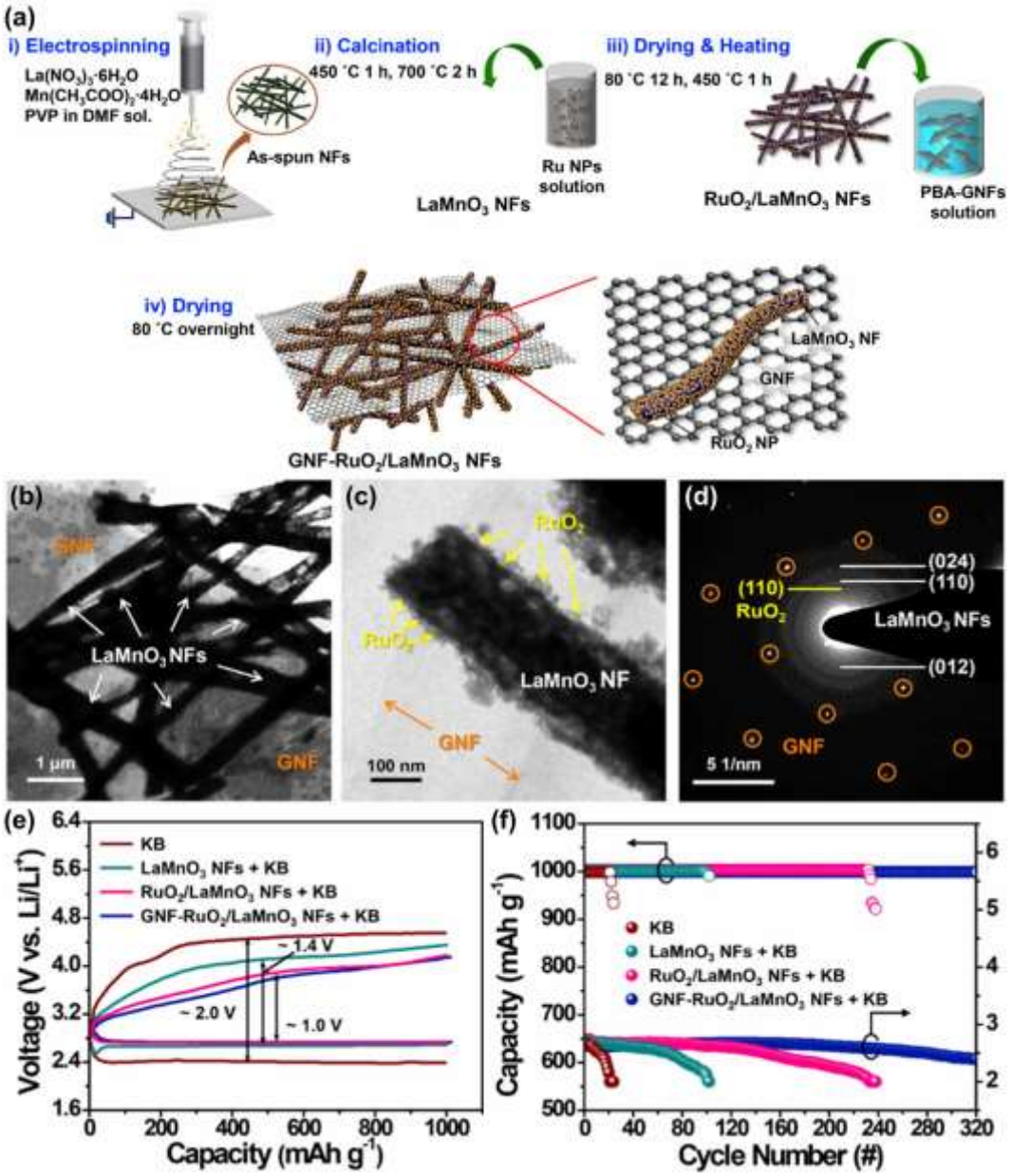

Figure 14. a) The synthetic route for $LaMnO_3$ NFs, $RuO_2/LaMnO_3$ NFs, and GNF-$RuO_2/LaMnO_3$ NFs. b-d) TEM images with b) low and c) high magnification. d) the selected-area diffraction (SAED) pattern of GNF-$RuO_2/LaMnO_3$ NFs. e) First discharge and charge voltage profiles. f) Cycle performance and terminal discharge voltages with a capacity limitation of 1000 mAh g^{-1} at a current density of 400 mAg^{-1} in the voltage range of 2.0–4.8 V. Reproduced with permission.[222] Copyright 2016, Wiley-VCH Verlag GmbH & Co. KGaA, Weinheim.

Table 1. Summary of the perovskite oxide nanoparticle used in non-aqueous lithium-oxygen batteries

Research issue	Perovskite oxide type	Grain size [nm]	Surface area [m^2 g^{-1}]	Electrolyte solvent	Current base [mA g^{-1}]	Discharge capacity [mAh g^{-1}]	Voltage [V]	Cycle condition [mAh g^{-1}]	Cycle life	Ref.
Direct use	$LaNiO_3$	<100	22.7	TEGDME	Carbon + Catalyst	7076	2.3	500	155	[171]
	$La_{0.6}Sr_{0.4}CoO_3$	80	4.55	EC/DEC	Carbon	3672	2.0−4.35	3672−581 1238−250 500	6 7 16	[192]
	$La_{0.6}Sr_{0.4}Co_{0.2}Fe_{0.8}O_3$	60	10.69	DMSO	-	20039	2.2−4.5	500	17	[133]
	$Ba_{0.9}Co_{0.5}Fe_{0.4}Nb_{0.1}O_{3-\delta}$	200[a]	10.24	EC/DMC	Electrode	1235[b]	2.0−4.5	1235−580	3	[193]
	$Ba_{0.9}Co_{0.7}Fe_{0.2}Nb_{0.1}O_{3-\delta}$	1000−2000	4.86	TEGDME	Electrode	11978.9	2.0−4.35	1000	24	[172]
Particle size and defect	$La_{0.8}Sr_{0.2}MnO_3$ $La_{0.8}Sr_{0.2}MnO_3$ (nano-sized)	1000−3000 100	1 32	EC/DMC	Carbon	1438 1922	2.0	-	-	[173]
	$La_{0.6}Sr_{0.4}CoO_{3-\delta}$ $La_{0.6}Sr_{0.4}CoO_{3-\delta}$ (BM-12 h)[c] $La_{0.6}Sr_{0.4}CoO_{3-\delta}$ (BM-24 h) $La_{0.6}Sr_{0.4}CoO_{3-\delta}$ (BM-36 h) $La_{0.6}Sr_{0.4}CoO_{3-\delta}$ (BM-48 h)	250 30−50 >50[a]	0.20 28.91 31.70 32.38 28.74	TEGDME	-	2094 2354 3256 2444 2142	2.0−4.3	500	28 34 43 33 32	[175]
A-site substitution	$La_{0.65}X_{0.35}MnO_3$ (X = Sr, Ba, Pb) $La_{0.65}Sr_{0.35}MnO_3$ $La_{0.65}Ba_{0.35}MnO_3$ $La_{0.65}Pb_{0.35}MnO_3$	200[a]	-	TEGDME	Electrode	6760 6205 7211	2.25−4.35	~960	20 18 35	[179]
B-site Substitution[d]	$LaNi_{1-x}\mathbf{Mg}_xO_3$ (x = 0, 0.08, 0.15) $LaNiO_3$ $LaNi_{0.92}Mg_{0.08}O_3$ $LaNi_{0.85}Mg_{0.15}O_3$	~100[a]	-	EC/DMC	-	300 490 620	2.0	-	-	[180]
	$La_{0.6}Sr_{0.4}Co_{1-x}\mathbf{Mn}_xO_3$ (x = 0, 0.05, 0.1) $La_{0.6}Sr_{0.4}CoO_3$ $La_{0.6}Sr_{0.4}Co_{0.95}Mn_{0.05}O_3$ $La_{0.6}Sr_{0.4}Co_{0.9}Mn_{0.1}O_3$	100−120	4.59	Tetramethylene sulfone	Carbon	2015 2378 3107	2.0−4.5	500−370 500−389	22 53	[181]
	$LaCo_{1-x}\mathbf{Ni}_xO_3$ (x = 0 ~ 1) $LaCoO_3$ $LaNi_{0.25}Co_{0.75}O_3$ $LaNi_{0.5}Co_{0.5}O_3$ $LaNi_{0.75}Co_{0.25}O_3$ $LaNiO_3$	100−200[a]	31.9 46.7 45.3 43.8 40.9	TEGDME	Electrode	3750 7720 (max) ~6440 ~5650 ~4260	2.0−4.1	1000	49	[184]
	$La_{0.6}Sr_{0.4}Co_{1-x}\mathbf{Ni}_xO_3$ (x = 0, 0.05, 0.1) $La_{0.6}Sr_{0.4}CoO_3$ $La_{0.6}Sr_{0.4}Co_{0.95}Ni_{0.05}O_3$ $La_{0.6}Sr_{0.4}Co_{0.9}Ni_{0.1}O_3$	100−120	-	EC/DEC	Carbon	1812 2190 2324	2.0−4.35	 500	 17	[182]
	$La_{0.8}Sr_{0.2}Mn_{1-x}\mathbf{Ni}_xO_3$ (x = 0, 0.2, 0.4) $La_{0.8}Sr_{0.2}MnO_3$ $La_{0.8}Sr_{0.2}Mn_{0.8}Ni_{0.2}O_3$ $La_{0.8}Sr_{0.2}Mn_{0.6}Ni_{0.4}O_3$	31.1 23.3 14.1	8.69 - 14.41	TEGDME	Carbon	4408 5364	2.2−4.5	500 500	54 79	[183]

[a]Estimated from the SEM image; [b]In the atmosphere composed of 20% O_2 and 80% N_2; [c]BM is short for ball milling; [d]Investigated element is in bold.

Table 2. Summary of perovskite oxides with various morphologies used in non-aqueous lithium-oxygen batteries

Perovskite oxide	Morphology	Fabrication method	Surface area [m^2 g^{-1}]	Electrolyte solvent	Current base [mA g^{-1}]	Discharge capacity [mAh g^{-1}]	Voltage [V]	Cycle condition [mAh g^{-1}]	Cycle number	Ref.
$La_{0.5}Sr_{0.5}CoO_{2.91}$	Nanowire (combined nanorodes)	Multistep microemulsion	96.78	EC/DMC	-	11059	2.0	-	-	[132]
$La_{0.5}Sr_{0.5}CoO_{2.91}$	Nanotube	Electrospinning	36.97	TEGDME	Carbon	7205	2.0−5.0	1000	85	[199]
$La_{0.5}Sr_{0.5}CoO_{3-\delta}$	Nanotube	Electrospinning	17.18	TEGDME	Carbon	5799	2.20−4.35 1.50−4.35	5799−4391 500	5 50	[198]
$La_{0.75}Sr_{0.25}MnO_3$	Nanotube	Electrospinning	31.34	TEGDME	Carbon	11000	2.2−4.4 2.2−4.4	11000−9000 1000	5 124	[197]
$La_{0.8}Sr_{0.2}MnO_3$	Nanorode	Soft template	20.6	TEGDME	Carbon + Catalyst	8890	2.2−4.4 2.67−4.4	7360−4160 1000	5 30	[200]
$LaNiO_3$	Nanocube	Hydrothermal reaction	35.8	TEGDME	Electrode	3407	2.0−4.3	1000 500	23 75	[201]

Perovskite oxides as the electrode materials in non-aqueous lithium-oxygen batteries have been reviewed. Future research directions of perovskite oxides should focus on the understanding of electrochemical mechanisms during the oxygen reduction and evolution processes, the structure design from nanoparticles to hierarchical porous structures, and the composite incorporation with improved electrical conductivities, catalytic activities, and structural merits.

Keyword perovskite oxide, oxygen electrode, non-aqueous lithium-oxygen battery, mechanism, structure

Peng Tan, Meilin Liu, Zongping Shao*, Meng Ni*

Recent advances in perovskite oxides as electrode materials for non-aqueous lithium-oxygen batteries